From Synchronisation to Persistent Optical Turbulence in Laser Arrays

Nicholas Blackbeard*, Sebastian Wieczorek, Hartmut Erzgräber, Partha Sharathi Dutta[1]

Mathematics Research Institute, University of Exeter, United Kingdom

Abstract

We define and study synchronisation in a linear array of nearest-neighbour coupled lasers. Our focus is on possible synchronisation types and the stability of their corresponding synchronisation manifolds with dependence on the coupling strength, the laser frequency detuning, the amount of shear (amplitude-phase coupling) in a single laser, and the array size. We classify, and give analytical conditions for the existence of complete synchronisation solutions, where all the lasers emit light with the same intensity and frequency. Furthermore, we derive stability criteria for two special cases where all the lasers oscillate (i) in-phase with each other and (ii) in anti-phase with their nearest neighbour(s). We then explain transitions from complete synchronisation, to partial synchronisation (where only a subset of the lasers synchronise), to persistent optical turbulence (where no lasers synchronise and each laser is chaotic) in terms of bifurcations including blowouts of chaotic attractors. Finally, we quantify properties of optical turbulence using Lyapunov spectrum and dimension, which highlights differences in chaos generated by nearest-neighbour and globally coupled oscillators.

Keywords: coupled lasers, synchronisation, optical turbulence, blowout bifurcation, intermittency, riddled basin
2000 MSC: 34C14, 34C15, 34C23, 34C30, 34C60

1. Introduction

Lasers are self-sustained nonlinear oscillators that are well described by low dimensional rate equation models [1, 2, 3] in the form of ordinary differential equations. When two or more lasers are coupled together in a *laser array* the resulting systems are rich in nonlinear phenomena [4, 5, 6, 7, 8, 9, 10, 11, 12, 13]. Nonlinear behaviour of laser arrays has been the

*Corresponding author. Present address: Tyndall National Institute, University College Cork, Ireland
Email addresses: nicholas.blackbeard@tyndall.ie (Nicholas Blackbeard), s.m.wieczorek@exeter.ac.uk (Sebastian Wieczorek), partha.sharathi.dutta@uni-oldenburg.de (Partha Sharathi Dutta)
[1]Present address: Institute for Chemistry and Biology of the Marine Environment, Carl von Ossietzky University Oldenburg, Germany

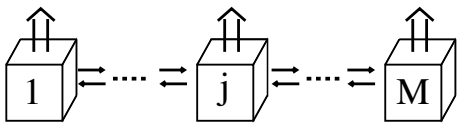

Figure 1: A schematic of M lasers with nearest-neighbour coupling and no periodic boundary conditions.

focus of many studies. From the practical viewpoint, laser arrays are used in various applications ranging from high-power light generation for industry [14, 15] to optical logic/memory elements [16]. From the theoretical viewpoint, they provide theoretical models and experimental setups for studying fundamental nonlinear phenomena such as various types of synchronisation [17, 18]. Despite much important previous work on the subject, many interesting aspects of nonlinear behaviour in laser arrays still remain unexplored. In this paper we study properties of synchronisation and the underlying mechanisms of synchronisation-desynchronisation transitions in linear arrays of laser oscillators. Each laser is evanescently coupled to its nearest neighbour(s) and the first and last lasers are uncoupled (Fig. 1).

Our study is motivated by two different behaviour types that we show in Fig. 2 for an array of 50 lasers. In Fig. 2(a) uniform stationary patterns are formed when all the lasers synchronise so that they emit light at the same frequency and the same constant intensity. We refer to this as *complete intensity synchronisation*. Such solutions are potentially useful for high-power light generation [14], and have been studied for laser arrays with different coupling types and geometries. Examples include nearest-neighbour coupling in circular arrays (periodic boundary conditions) [19, 20, 21, 22] and linear arrays (no periodic boundary conditions) [23, 20], as well as global coupling [20, 21, 24, 25] with time delay [26]. In particular, Winful and Rahman [23] derived stability conditions for in-phase and anti-phase (π out-of-phase) intensity synchronisation for two coupled lasers. Li and Erneux [20] extended these results to an arbitrary number of lasers in a circular array with nearest-neighbour and global coupling. Nonetheless, synchronisation conditions for commercially available linear arrays such as the one in Fig. 1 have not been studied. In contrast to intensity synchronisation, Fig. 2(b) shows a complicated non-stationary pattern that is formed when each laser is chaotic in time and there is no synchronisation (defined in § 3 ahead) between any lasers. This is an example of what we refer to as *optical turbulence*. Such solutions have been mentioned by Otsuka [19] and are potentially useful for modern applications including chaos-based laser radars [27], secure communication schemes [28, 29], and ultra-fast random number generation [30], all of which require persistent and intense chaos.

Here, we combine techniques from stability analysis of invariant synchronisation manifolds and equivariant bifurcation theory to expand on previous results and uncover new phenomena associated with synchronisation in linear laser arrays. More specifically, we identify possible types of intensity synchronised solutions and various configurations within the linear array (symmetric and asymmetric) that allow such solutions. Next, we give analytical conditions for the stability of intensity synchronised solutions where each laser emits in phase and in anti-phase with its neighbour(s). Furthermore, we show that transitions from complete intensity synchronisation to optical turbulence may involve various codimension-one

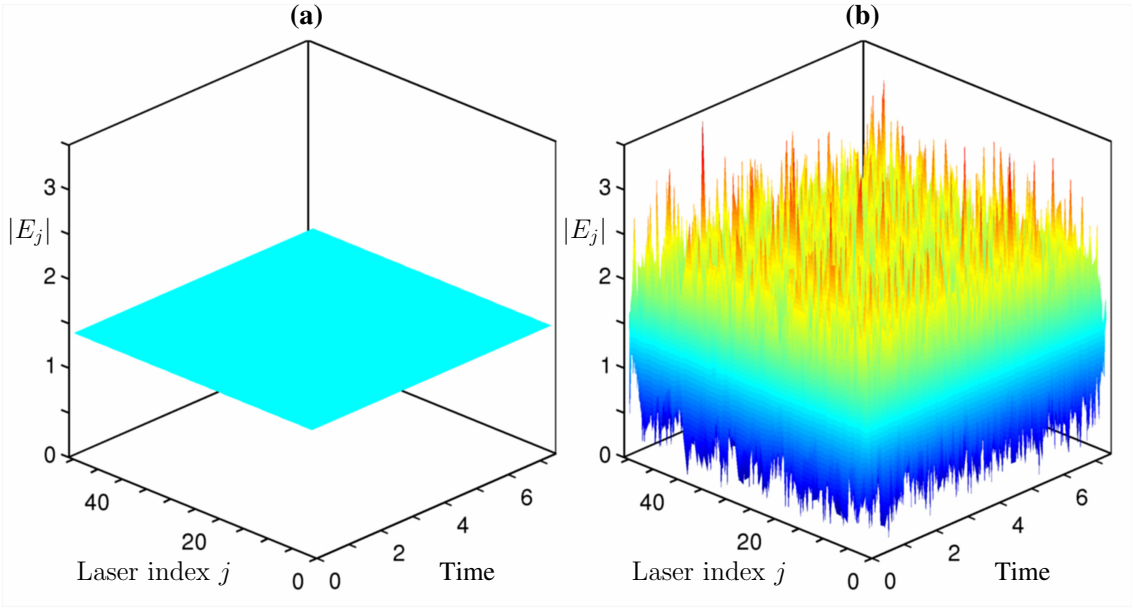

Figure 2: Colour online. Contrasting dynamics in an array of 50 lasers with nearest-neighbour coupling. The distribution of natural frequencies, Δ_j, is such that $\Delta_1 = \Delta_{50} = \Delta_{out}$ and $\Delta_2 = \cdots = \Delta_{49} = \Delta_{in}$. (a) Complete intensity synchronisation where each laser is in anti-phase with its nearest neighbour(s) ($\alpha = 2$, $\kappa = 1$ and $\Delta_{in} = \Delta_{out} - 1$). (b) Optical turbulence where no lasers are synchronised and each laser is chaotic ($\alpha = 5$, $\kappa = 30$ and $\Delta_{in} = \Delta_{out}$).

and -two bifurcations, and focus on those that are due to bifurcations of chaotic attractors. Finally, we study persistence and intensity of optical turbulence in terms of Lyapunov spectrum, and uncover differences between chaotic behaviour of nearest-neighbour and globally coupled oscillators.

This paper is organised as follows. In § 2 we introduce the coupled-laser model. A definition of laser synchronisation is given in § 3. In § 4 we discuss the symmetries of the coupled-laser model in relation to laser synchronisation. Our main results start in § 5 where we study, analytically, possible intensity-synchronised solutions (such as the one in Fig. 2(a)) and their stability. Then, in § 6 we study, numerically, different transitions from complete synchronisation (where all the lasers synchronise) to optical turbulence (where no lasers synchronise and each laser is chaotic in time), assuming a particular distribution of natural frequencies. First we focus on an array of three laser oscillators and then show how the results are modified for larger arrays. In § 7 we use the Lyapunov spectrum of the underlying chaotic attractors to study persistence, intensity, and dimensionality of chaos with dependence on the coupling strength and array size. Finally, § 8 summarises our results.

Parameter	Description	Value
γ	Ratio of field and population decay rates	100
β	Normalised gain coefficient	5.16
Λ	Normalised pump rate	2
κ	Normalised coupling strength	$[0, 100]$
$\Delta = \Omega_{in} - \Omega_{out}$	Normalised frequency detuning	$[-30, 30]$
α	Linewidth enhancement factor (shear)	$[0, 5]$

Table 1: Laser parameters and their values [10].

2. Coupled-Laser Equations

A solitary class-B laser [31, 32] is a self-sustained, three-dimensional, nonlinear oscillator whose dynamics can be described by *rate equations* of the form

$$\frac{dE}{dt} = -i\Delta\, E + \beta\gamma(1 - i\alpha)\, N\, E, \tag{1}$$

$$\frac{dN}{dt} = \Lambda - N - (1 + \beta N)|E|^2, \tag{2}$$

where $E(t) = A(t) + iB(t)$ is the (normalised) complex-valued electric field, and $N(t)$ is the (normalised) real-valued population inversion within the laser active medium. Throughout the paper, we will often refer to (normalised) *laser intensity* which is equal to $|E(t)|^2$. Parameters such as the normalised gain coefficient, β, the ratio of photon and population-inversion decay rates, γ, and the normalised pump rate, Λ, are kept constant at typical values given in Table 1. The normalised frequency detuning, Δ, is the difference between the laser natural frequency and a suitably chosen reference frequency, in units of the population-inversion decay rate. The linewidth enhancement factor, α, quantifies an important nonlinear property of (semiconductor) lasers — strong coupling between the magnitude and phase of the lasing field E. Such coupling leads to magnitude-dependent frequency also known as *non-isochronicity* or *shear* [33, Ch. 7.1]. A single laser above its lasing threshold ($\Lambda > 0$) has a stable limit cycle given by $|E(t)|^2 = \Lambda$ and $N(t) = 0$.

To simplify notation for laser arrays we introduce a three-dimensional state vector $\mathbf{x}(t) = (A(t), B(t), N(t))^T$ and rewrite (1) and (2) as

$$\frac{d\mathbf{x}}{dt} = \mathbf{f}(\mathbf{x}), \tag{3}$$

where the vector field $\mathbf{f}$ is given by

$$\mathbf{f}(\mathbf{x}(t)) = \begin{pmatrix} \beta\gamma N(t)(A(t) + \alpha B(t)) + \Delta B(t) \\ \beta\gamma N(t)(B(t) - \alpha A(t)) - \Delta A(t) \\ \Lambda - N(t) - (1 + \beta N(t))(A(t)^2 + B(t)^2) \end{pmatrix}. \tag{4}$$

Then, laser arrays are described by ordinary differential equations of the form

$$\frac{d\mathbf{x}_j}{dt} = \mathbf{f}_j(\mathbf{x}_j) + \kappa \sum_{j'=1}^{M} G_{jj'} \mathbf{H} \mathbf{x}_{j'}, \tag{5}$$

where $j = 1, \cdots, M$ is the laser index. The coupling between lasers is assumed to be of equal strength, κ, and through the same linear combination of the laser variables,

$$\mathbf{H} = \begin{pmatrix} 0 & -1 & 0 \\ 1 & 0 & 0 \\ 0 & 0 & 0 \end{pmatrix}. \tag{6}$$

Such $\mathbf{H}$ means that coupling terms in the form $i\kappa E_{j'}$ are added to the right-hand side of (1), which has been shown in Refs. [34, 35] to be consistent with the solution of Maxwell's equations and the relevant boundary conditions. We would like to remark that other forms of coupling terms have been used in the literature, some of which even lead to unbounded solutions as pointed out in Ref. [35]. The coupling configuration is described by the elements of the $M \times M$ *connectivity matrix*, $G_{jj'}$. This paper studies a linear array with nearest-neighbour coupling as shown in Fig. 1, meaning that

$$G_{jj'} = \begin{cases} 1 & \text{if } |j - j'| = 1, \\ 0 & \text{otherwise.} \end{cases} \tag{7}$$

Although the lasers are not diffusively coupled, the coupled-laser equations (5) are easily transformed into the widely studied form of *diffusive coupling* by replacing Δ_j with

$$\hat{\Delta}_j = \begin{cases} \Delta_j - \kappa & \text{if } j = 1, M, \\ \Delta_j - 2\kappa & \text{if } 1 < j < M, \end{cases}$$

and replacing $G_{jj'}$ with the *diffusive connectivity matrix*

$$\hat{G}_{jj'} = \begin{cases} -1 & \text{if } j = j' = 1, M, \\ -2 & \text{if } 1 < j = j' < M, \\ G_{jj'} & \text{otherwise.} \end{cases} \tag{8}$$

Throughout this paper, individual lasers in the array are assumed to be identical ($\beta_j = \beta$, $\gamma_j = \gamma$, $\Lambda_j = \Lambda$, and $\alpha_j = \alpha$ for $j = 1, \cdots, M$) except for a possible difference in their natural frequencies, meaning that Δ_j and $\Delta_{j' \neq j}$ need not be the same. Our focus is on synchronisation types and different synchronisation-desynchronisation transitions in the coupled-laser model (5) with dependence on the coupling strength, κ, frequency detuning between certain lasers, and the amount of shear in a single laser, α.

3. Laser Synchronisation and Phase-Locking

When lasers are coupled together it is natural to ask if some form of synchronisation [36, 33] is possible. We say that lasers j and j' are *synchronised* if two conditions are satisfied. Firstly, there exists a stable, fixed-in-time relationship between their electric fields such that

$$c_j E_j(t) - c_{j'} E_{j'}(t) = 0, \tag{9}$$

for some constants $c_j, c_{j'} \in \mathbb{C}$. Secondly, this relationship is attractive meaning that

$$\lim_{t\to\infty} (c_j E_j(t) - c_{j'} E_{j'}(t)) = 0, \tag{10}$$

for all initial conditions within some $3M$-dimensional subset of the phase space.

A particular type of synchronisation called *n:m phase locking* is often considered in the literature. For this one needs to define a suitable phase variable of an oscillator [33, Ch. 2]. The phase of a laser oscillator can be defined straightforwardly as $\phi_j(t) = \arg(E_j(t))$. We say that lasers j and j' are *1:1 phase-locked* (or simply *locked*) if there is a fixed-in-time relationship between their phases, and this relationship is attractive:

$$\lim_{t\to\infty} (\phi_{jj'}(t) \equiv \phi_j(t) - \phi_{j'}(t)) = \text{const. } \mathrm{mod}\, 2\pi\,. \tag{11}$$

Notice that if two lasers are synchronised (9)–(10) then they are also locked (11).

Furthermore, we distinguish between different types of synchronisation depending on the number of lasers that are synchronised, and the relationships between their phases and magnitudes. If all the lasers are synchronised we speak of *complete synchronisation*, but if only a subset of the lasers are synchronised we have *partial synchronisation*. Given (9)–(10), we speak of *in-phase synchronisation* if $\phi_{jj'} = 0$, *anti-phase synchronisation* if $\phi_{jj'} = \pi$, and *out-of-phase synchronisation* otherwise. Finally, if the electric field magnitudes for lasers j and j' are identical, $|E_j(t)| = |E_{j'}(t)|$, then we say that the lasers are *intensity synchronised*.

4. Symmetries and their Role in Synchronisation

The vector field $\mathbf{f}_j$ describing the dynamics of a solitary laser is rotationally symmetric (equivariant) under phase shifting $E_j(t)$ by a constant θ_j,

$$T: \quad E_j \to e^{i\theta_j} E_j \quad \text{for} \quad \theta_j \in [0, 2\pi)\,.$$

This transformation can be represented by the 3×3 matrix

$$\mathbf{R}_j = \begin{pmatrix} \cos\theta_j & -\sin\theta_j & 0 \\ \sin\theta_j & \cos\theta_j & 0 \\ 0 & 0 & 1 \end{pmatrix}, \tag{12}$$

and we refer to $\mathbf{R}_j$ as an *internal symmetry* of laser j. If $\kappa = 0$ then the coupled-laser model (5) has $\prod_{j=1}^{M} \mathbb{S}^1$ symmetry due to the M rotational symmetries of the individual lasers. This is represented by the $3M \times 3M$ matrix

$$\mathbf{R} = \begin{pmatrix} \mathbf{R}_1 & \mathbf{0} & \cdots & \mathbf{0} \\ \mathbf{0} & \mathbf{R}_2 & \ddots & \vdots \\ \vdots & \ddots & \ddots & \mathbf{0} \\ \mathbf{0} & \cdots & \mathbf{0} & \mathbf{R}_M \end{pmatrix}. \tag{13}$$

	Solution of full system contained in Fix($\mathbb{Z}_2$)	Coupling structure for the $\mathbb{Z}_2$-restricted system
Odd number of lasers $M = 2L - 1$		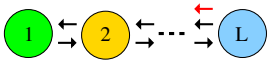
Even number of lasers $M = 2L$	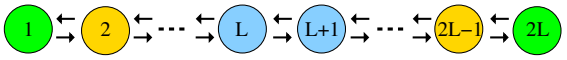	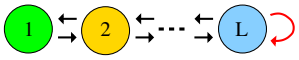

Table 2: Colour online. Dynamical properties associated with the fixed-point subspace. Shades/colours in the second column indicate which lasers (circles) are necessarily intensity and in-phase synchronised if a solution of the full system (5) is contained in Fix($\mathbb{Z}_2$). The third column shows the coupling structure between L lasers in the restriction of the full system to Fix($\mathbb{Z}_2$).

However, if $\kappa > 0$ then the coupled-laser model (5) has only $\mathbb{S}^1$ symmetry which is also represented by the matrix transformation $\mathbf{R}$ but with $\theta_j = \theta$ for all j. In this case the simplest nonzero asymptotic solutions lie on $\mathbb{S}^1$-group orbits and are typically limit cycles. Such solutions are given by

$$\begin{aligned} E_j(t) &= |E_j^0| e^{i(\omega t + \varphi_j^0)}, \\ N_j(t) &= N_j^0, \end{aligned} \tag{14}$$

for $j = 1, \cdots, M$, where $|E_j^0|$, φ_j^0, ω, and N_j^0 are real constants. When these solutions are stable they represent a form of complete synchronisation where all the lasers phase-lock (11) to the same optical frequency ω. A group orbit reduction can be used to obtain a $\mathbb{S}^1$-*reduced system* with the $\mathbb{S}^1$ symmetry removed [13]. Synchronised solutions (14) are studied as isolated equilibria in the $\mathbb{S}^1$-reduced system which greatly facilitates analytical and numerical stability analysis.

In this paper we will consider cases where the coupled-laser model (5) also has (reflectional) $\mathbb{Z}_2$ symmetry, meaning that its right-hand side is equivariant under the transformation

$$\begin{aligned} T_{\mathbb{Z}_2} : E_j &\to E_{M-j+1}, \\ N_j &\to N_{M-j+1}, \end{aligned}$$

for $j = 1, \cdots, M$. The $\mathbb{Z}_2$ symmetry implies the existence of an invariant manifold called the *fixed-point subspace* [37],

$$\text{Fix}(\mathbb{Z}_2) = \{(\mathbf{x}_1, \cdots, \mathbf{x}_M)^T \in \mathbb{R}^{3M} \ : \ \mathbf{x}_j = \mathbf{x}_{M-j+1} \text{ for } j = 1, \cdots, M\}. \tag{15}$$

The dynamics within Fix($\mathbb{Z}_2$) is governed by the $\mathbb{Z}_2$-*restricted system* which is obtained by setting $\mathbf{x}_j = \mathbf{x}_{M-j+1}$ for $j = 1, \cdots, M$ in the full system (5).

On the invariant manifold Fix($\mathbb{Z}_2$), pairs of lasers are synchronised with each other and identical shades/colours in Table 2 show which lasers (represented by circles) are necessarily intensity and in-phase synchronised. There is a subtle difference between arrays of odd and even lasers. For $M = 2L - 1$ odd, there is a unique middle laser $j = L$ which need not be synchronised with any other laser, whereas for $M = 2L$ even, no such laser exists. This

difference shows up in the $\mathbb{Z}_2$-restricted system. In both cases the restricted system describes the dynamics of L coupled lasers but with different coupling terms as indicated by the extra (red) arrows in the third column of Table 2. For M odd, coupling from laser L to laser $L-1$ is twice stronger than coupling from laser $L-1$ to laser L. For M even, coupling between different lasers is equally strong but laser L is also coupled to itself.

5. Complete Intensity Synchronisation

In this section we study complete intensity synchronisation where all lasers have identical electric field magnitudes:

$$|E_1(t)| = \cdots = |E_M(t)| = |E_s(t)|. \tag{16}$$

The analysis is performed in two steps. First, we derive conditions for the existence of different synchronised solutions, and classify different types of complete intensity synchronisation. Then, we give conditions for the synchronised solutions to be stable and identify mechanisms responsible for synchronisation-desynchronisation transitions.

5.1. Existence of Synchronised Solutions and Manifolds

The aim of this section is to find all solutions of the M coupled-laser model (5) that satisfy the complete intensity synchronisation condition (16), meaning that the c_j's in (9)–(10) become $c_j = e^{i\theta_j}$ for $j = 1, \cdots, M$. Let us assume a *synchronised solution* of the form

$$e^{i\theta_1} E_1(t) = \cdots = e^{i\theta_M} E_M(t) = E_s(t)\,, \tag{17}$$

for all time t, where $E_s(t)$ is non-zero. Differentiating the above equation with respect to time shows that (17) implies

$$e^{i\theta_j} \frac{dE_j}{dt} = e^{i\theta_{j'}} \frac{dE_{j'}}{dt} = \frac{dE_s}{dt}\,, \tag{18}$$

for $j, j' \in \{1, \cdots, M\}$ and all t. Using (5) for the first two components of $\mathbf{x}_j$ and $\mathbf{f}_j(\mathbf{x}_j)$, substituting (17), and taking the real and imaginary parts of (18) gives

$$\begin{aligned} N_j(t) - N_{j'}(t) &= \frac{-1}{\beta\gamma(1-\alpha^2)} \left(\alpha(\Delta_j - \Delta_{j'}) - \kappa(\alpha a_{jj'} + b_{jj'})\right), \\ 0 &= \frac{1}{\beta\gamma(1-\alpha^2)} \left((\Delta_j - \Delta_{j'}) - \kappa(a_{jj'} - \alpha b_{jj'})\right)\,, \end{aligned} \tag{19}$$

where

$$a_{jj'} + i b_{jj'} = \sum_{j''=1}^{M} (G_{jj''} e^{i\theta_{j,j''}} - G_{j'j''} e^{i\theta_{j',j''}})\,,$$

and $\theta_{j,j'} = \theta_j - \theta_{j'}$. Furthermore, noting that the right-hand side of (19) does not vary in time, comparing the time derivative of (19) with (2), and using (17) gives

$$-(N_j(t) - N_{j'}(t))(1 + \beta|E_s(t)|^2) = 0\,, \tag{20}$$

for $j, j' \in \{1, \cdots, M\}$ and all t. Equation (20) holds if and only if

$$N_1(t) = \cdots = N_M(t) = N_s(t)\,, \tag{21}$$

for all t, which implies that

$$\frac{dN_1}{dt} = \cdots = \frac{dN_M}{dt} = \frac{dN_s}{dt}. \tag{22}$$

So far, we have shown by taking the real part of (18) that complete intensity synchronisation (17) implies equal levels of population inversion in all the lasers (21). The next step is to derive the corresponding conditions for θ_j and Δ_j that need to be satisfied for synchronised solutions (17) to exist.

To make the analysis more general and to facilitate the presentation of our results we use the internal symmetries $\mathbf{R}_j$ to define new variables

$$\mathbf{y}_j = \mathbf{R}_j \mathbf{x}_j\,,$$

and rewrite the M coupled-laser model (5) as

$$\frac{d\mathbf{y}_j}{dt} = \mathbf{f}_j(\mathbf{y}_j) + \kappa \sum_{j'=1}^{M} G_{jj'} \mathbf{R}_j \mathbf{H} \mathbf{R}_{j'}^{-1} \mathbf{y}_{j'}\,, \tag{23}$$

for $j = 1, \cdots, M$. Furthermore, we rewrite the synchronised solution (17) and (21) as

$$\mathbf{y}_1 = \cdots = \mathbf{y}_M = \mathbf{y}_s\,, \tag{24}$$

and conditions (18) and (22) as

$$\frac{d\mathbf{y}_1}{dt} = \cdots = \frac{d\mathbf{y}_M}{dt} = \frac{d\mathbf{y}_s}{dt}\,. \tag{25}$$

It now becomes clear that if (24) is satisfied for some initial time t_0 and (25) is satisfied for all t, then the synchronised solution $\mathbf{y}_s$ defined by (24) exists for all t. To satisfy (25) for all t we require that

$$\mathbf{f}_j(\mathbf{y}_s) - \mathbf{f}_{j'}(\mathbf{y}_s) = \kappa \sum_{j''=1}^{M} \left(G_{j'j''} \mathbf{R}_{j'} \mathbf{H} \mathbf{R}_{j''}^{-1} - G_{jj''} \mathbf{R}_j \mathbf{H} \mathbf{R}_{j''}^{-1} \right) \mathbf{y}_s\,, \tag{26}$$

for $j, j' \in \{1, \cdots, M\}$. Setting $j' = 1$ and using matrices (6) and (7), condition (26) can be expressed in terms of $(M-1)$ equations:

$$(\Delta_1 - \Delta_j)\mathbf{H}\mathbf{y}_s = \kappa \left(\mathbf{R}_1 \mathbf{R}_2^{-1} - \mathbf{R}_j \mathbf{R}_{j-1}^{-1} - \hat{\delta}_{jM} \mathbf{R}_j \mathbf{R}_{j+1}^{-1} \right) \mathbf{H}\mathbf{y}_s\,, \tag{27}$$

where $j = 2, \cdots, M$ and $\hat{\delta}_{jM} = 1 - \delta_{jM}$. Alternatively, (27) can be viewed as $(M-1)$ eigenvalue problems:

$$\lambda_j \mathbf{v} = \mathbf{A}_j \mathbf{v}\,,$$

where $\lambda_j = (\Delta_1 - \Delta_j)/\kappa$, $\mathbf{v} \in \mathbb{R}^2$, $\mathbf{A}_j$ is the 2×2 matrix

$$\mathbf{A}_j = \begin{pmatrix} \cos\theta_{1,2} - \cos\theta_{j,j-1} - \hat{\delta}_{jM}\cos\theta_{j,j+1} & -\sin\theta_{1,2} + \sin\theta_{j,j-1} + \hat{\delta}_{jM}\sin\theta_{j,j+1} \\ \sin\theta_{1,2} - \sin\theta_{j,j-1} - \hat{\delta}_{jM}\sin\theta_{j,j+1} & \cos\theta_{1,2} - \cos\theta_{j,j-1} - \hat{\delta}_{jM}\cos\theta_{j,j+1} \end{pmatrix},$$

and $\theta_{j,j'} = \theta_j - \theta_{j'}$. The corresponding $(M-1)$ eigenvalues are given by

$$\begin{aligned} \frac{\Delta_1 - \Delta_j}{\kappa} &= \cos\theta_{1,2} - \cos\theta_{j,j-1} - \hat{\delta}_{jM}\cos\theta_{j,j+1} + \\ &\quad i(\sin\theta_{1,2} - \sin\theta_{j,j-1} - \hat{\delta}_{jM}\sin\theta_{j,j+1})\,, \end{aligned} \tag{28}$$

with $j = 2, \cdots, M$. Taking the imaginary part of (28) gives

$$\hat{\delta}_{jM}\sin\theta_{j,j+1} = \sin\theta_{1,2} - \sin\theta_{j,j-1}\,, \tag{29}$$

for $j = 2, \cdots, M$. One can show, using induction for $j = 2, \cdots, M-1$, that (29) implies

$$\sin\theta_{1,2} = \begin{cases} \frac{1}{j}\sin\theta_{j,j+1} & \text{for } j = 2, \cdots, M-1\,, \\ \sin\theta_{M,M-1} & \text{for } j = M\,. \end{cases} \tag{30}$$

Setting $j = M-1$ in (30) gives $\sin\theta_{1,2} = 0$, which then implies that

$$\theta_j - \theta_{j+1} = K_j\pi \bmod 2\pi\,, \tag{31}$$

for $K_j \in \{0, 1\}$ and $j = 1, \cdots, M-1$. Taking the real part of (28) and using (31) gives

$$\Delta_1 - \Delta_j = \kappa\left[(-1)^{K_1} - (-1)^{K_{j-1}} - \hat{\delta}_{jM}(-1)^{K_j}\right], \tag{32}$$

for $j = 2, \cdots, M$. Note that each synchronised solution is characterised by a different choice of K_j's in (31), which fixes the corresponding conditions (32) for the Δ_j's. Conversely, an allowed combination of Δ_j's imposes certain phase conditions in (31). These results mean that complete intensity synchronisation (17) allows for a difference of an integer multiple of π between the phases of any two neighbouring lasers (31), but requires the corresponding relation between the frequencies of individual lasers (32).

Possible combinations of Δ_j's in (32) reveal that intensity synchronised solutions arise in two system types: symmetric and asymmetric. If the Δ_j's satisfy the pattern in the second column of Table 2 then the system has $\mathbb{Z}_2$ symmetry and there are two possibilities for solution (17). Firstly, (17) may have $\mathbb{Z}_2$ symmetry in which case the θ_j's also satisfy the pattern in the second column of Table 2. Secondly, (17) may not have the symmetry in which case the θ_j's do not satisfy the pattern in the second column of Table 2; such

solutions are also found through embedding the linear array in a circular array with twice the number of lasers, and identifying solutions of the circular array that restrict to solutions of the original linear array [38]. If the system does not have $\mathbb{Z}_2$ symmetry then solution (17) does not have the symmetry either. For example, an asymmetric system with $M = 3$ and $\Delta_1 + \kappa = \Delta_2 = \Delta_3 - \kappa$, has just one synchronous solution (17), $E_1(t) = -E_2(t) = -E_3(t)$, which is asymmetric.

The synchronised solution condition (24) defines a three-dimensional invariant manifold:

$$\mathcal{M}_s = \{\mathbf{Y} = (\mathbf{y}_1, \cdots, \mathbf{y}_M)^T \in \mathbb{R}^{3M} : \mathbf{y}_1 = \cdots = \mathbf{y}_M = \mathbf{y}_s\}\,, \tag{33}$$

that is referred to as the *synchronisation manifold* [39]. Within the synchronisation manifold, Eqs. (23) reduce to the solitary-laser equations (1)–(2) with a modified frequency detuning. The concept of a synchronisation manifold facilitates the stability analysis performed in the next sections.

5.2. Stability of Special Synchronised Solutions

We are interested in the stability of two special cases of synchronised solutions that are found in numerical simulations, are potentially interesting for applications, and can be treated analytically. The first case, given by setting $K_j = K = 0$ for all j in (31), describes a situation where all the lasers are intensity synchronised and emit in-phase with each other:

$$E_1(t) = \cdots = E_M(t) = E_s(t)\,. \tag{34}$$

Using (32), such solutions require that

$$\Delta_1 = \Delta_M = \Delta_{out}\,, \tag{35}$$

$$\Delta_j = \Delta_{in}\,, \tag{36}$$

for $j = 2, \cdots, M-1$, and

$$\Delta_{in} - \Delta_{out} = \kappa\,. \tag{37}$$

The second case, given by setting $K_j = K = 1$ for all j in (31), describes a situation where all lasers are intensity synchronised and each laser emits in anti-phase with its neighbour(s):

$$E_1(t) = -E_2(t) = \cdots = (-1)^{M-1} E_M(t) = E_s(t)\,. \tag{38}$$

Using (32), this requires that (35) and (36) are satisfied but with

$$\Delta_{in} - \Delta_{out} = -\kappa\,. \tag{39}$$

The conditions on the Δ_j's namely (35)–(36) and (37), or (35)–(36) and (39), guarantee the existence of synchronised solutions of the forms (34) and (38), respectively. However, they do not imply laser synchronisation as defined in (9)–(10). For this, synchronised solutions need to be stable in the directions transverse to the corresponding synchronisation manifold.

With θ_j's satisfying (31) for $K_j = K \in \{0, 1\}$, equation (23) can be written as

$$\frac{d\mathbf{y}_j}{dt} = \mathbf{f}_j(\mathbf{y}_j) + \kappa \sum_{j'=1}^{M} G_{jj'} \mathbf{R}_K \mathbf{H} \mathbf{y}_{j'} \,, \tag{40}$$

where we used (31) to introduce

$$\mathbf{R}_K = \mathbf{R}_j \mathbf{R}_{j\pm1}^{-1} = \begin{pmatrix} (-1)^K & 0 & 0 \\ 0 & (-1)^K & 0 \\ 0 & 0 & 1 \end{pmatrix} . \tag{41}$$

Then, (40) can be rewritten as

$$\frac{d\mathbf{y}_j}{dt} = \mathbf{f}_j(\mathbf{y}_j) + \kappa n_j \mathbf{R}_K \mathbf{H} \mathbf{y}_j + \kappa \sum_{j'=1}^{M} \hat{G}_{jj'} \mathbf{R}_K \mathbf{H} \mathbf{y}_{j'} \,, \tag{42}$$

where $\hat{G}_{jj'}$ are elements of the diffusive connectivity matrix (8), and $n_j = \sum_{j'=1}^{M} G_{jj'}$ is the number of inputs that laser j receives from its neighbours. Furthermore, we introduce

$$\mathbf{f}_K(\mathbf{y}_j) = \mathbf{f}_j(\mathbf{y}_j) + \kappa n_j \mathbf{R}_K \mathbf{H} \mathbf{y}_j \,, \tag{43}$$

for $j = 1, \cdots, M$, and rewrite (42) as

$$\frac{d\mathbf{y}_j}{dt} = \mathbf{f}_K(\mathbf{y}_j) + \kappa \sum_{j'=1}^{M} \hat{G}_{jj'} \mathbf{R}_K \mathbf{H} \mathbf{y}_j \,, \tag{44}$$

for $j = 1, \cdots, M$. On the synchronisation manifold $\mathcal{M}_s$, (44) reduces to

$$\frac{d\mathbf{y}_s}{dt} = \mathbf{f}_K(\mathbf{y}_s) \,, \tag{45}$$

because $\sum_{j'} \hat{G}_{jj'} = 0$. One can check that for $\Lambda > 0$ there is a limit cycle:

$$\mathbf{y}_s(t) = (\sqrt{\Lambda}\cos(\varphi_K t), \sqrt{\Lambda}\sin(\varphi_K t), 0)^T, \tag{46}$$

where

$$\varphi_K = -\Delta_{out} + \kappa(-1)^K.$$

This limit cycle is stable within the synchronisation manifold. Next we want to know whether the limit cycle is stable to perturbations transverse to $\mathcal{M}_s$. For this it is convenient to write (44) in matrix notation

$$\frac{d\mathbf{Y}}{dt} = \mathbf{F}(\mathbf{Y}) + \kappa(\hat{\mathbf{G}} \otimes \mathbf{R}_K \mathbf{H})\mathbf{Y} \,, \tag{47}$$

where $\mathbf{Y} = (\mathbf{y}_1, \cdots, \mathbf{y}_M)^T \in \mathbb{R}^{3M}$, $\mathbf{F}(\mathbf{Y}) = (\mathbf{f}_K(\mathbf{y}_1), \cdots, \mathbf{f}_K(\mathbf{y}_M))^T$, and $\otimes$ is the Kronecker product. A synchronised solution, $\mathbf{y}_j(t) = \mathbf{y}_s(t)$ for $j = 1, \cdots, M$, is written as

$$\mathbf{Y}_s(t) = (\mathbf{y}_s(t), \cdots, \mathbf{y}_s(t))^T \in R^{3M} .$$

Let $\delta(t) = (\delta_1(t), \cdots, \delta_M(t))^T \in \mathbb{R}^{3M}$ denote an arbitrary perturbation vector. Making the substitution $\mathbf{Y}(t) = \mathbf{Y}_s(t) + \delta(t)$, Taylor expanding (47) about $\mathbf{Y}_s(t)$, and neglecting higher order terms gives the linearised variational equation

$$\frac{d\delta}{dt} = \left(\mathbf{I}_M \otimes \mathbf{Df}_K(\mathbf{y}_s(t)) + \kappa\hat{\mathbf{G}} \otimes \mathbf{R}_K\mathbf{H}\right)\delta(t) , \tag{48}$$

where $\mathbf{Df}_K(\mathbf{y}_s(t))$ is the Jacobian of $\mathbf{f}_K$ evaluated at $\mathbf{y}_s(t)$, and $\mathbf{I}_M$ is the $M \times M$ identity matrix. To identify perturbations in directions transverse and tangential to $\mathcal{M}_s$ we diagonalise $\hat{\mathbf{G}}$ by introducing ([40, pg. 394–396] and [41])

$$\xi(t) = (\mathbf{T} \otimes \mathbf{I}_3)\delta(t) , \tag{49}$$

where $\mathbf{T}$ is a 3×3 matrix whose columns are the eigenvectors of $\hat{\mathbf{G}}$, and rewrite (48) in terms of eigenvalues λ_j of $\hat{\mathbf{G}}$ as

$$\frac{d\xi_j}{dt} = \left(\mathbf{Df}_K(\mathbf{y}_s(t)) + \kappa\lambda_j\mathbf{R}_K\mathbf{H}\right)\xi_j(t) , \tag{50}$$

where $\xi_j \in \mathbb{R}^3$ and [42, 43]

$$\lambda_j = -4\sin^2\left(\frac{(j-1)\pi}{2M}\right) ,$$

for $j = 1, \cdots, M$. A comparison of (50) with (45) shows that $\lambda_1 = 0$ gives the variational equation for the perturbations within $\mathcal{M}_s$, while the remaining $\lambda_j \neq 0$ correspond to the time evolution of perturbations transverse to $\mathcal{M}_s$. In general, the synchronised solution, $\mathbf{y}_s(t)$, is time varying and hence (50) needs to be solved numerically [41]. However, if $\mathbf{y}_s(t)$ is an equilibrium then it may be possible to determine the stability exactly. Owing to the rotational $\mathbb{S}^1$ symmetry of laser oscillators, setting $\Delta_{out} = \kappa(-1)^K$ 'freezes' the limit cycle (46) into a circle of nonhyperbolic equilibria. We can linearise about any of these equilibria and for convenience we choose $\mathbf{y}_s(t) = (\sqrt{\Lambda}, 0, 0)^T$. Then, the characteristic equation for (50) is

$$s^3 + s^2(1 + \beta\Lambda) + s(\lambda_j^2\kappa^2 + 2\beta\gamma\Lambda) + \lambda_j^2\kappa^2(1 + \beta\Lambda) + 2\lambda_j\alpha\beta\gamma\kappa\Lambda(-1)^K = 0 . \tag{51}$$

Synchronised solutions (46) are transversally stable if all roots s of Eqn. (51) with $j = 2, \cdots, M$ lie in the negative half-plane. Using the Routh–Hurwitz criterion [44, Ch. 1] this requires that

$$\kappa\lambda_j(-1)^K \;<\; \frac{1 + \beta\Lambda}{\alpha} , \tag{52}$$

and

$$\kappa \;>\; \frac{-(-1)^K 2\alpha\beta\gamma\Lambda}{\lambda_j(1+\beta\Lambda)}\,, \tag{53}$$

for $j = 2, \cdots, M$.

Now the two special cases, $K = 0$ and $K = 1$, are treated separately. For $K = 0$, inequality (52) is always satisfied and the necessary and sufficient condition for (46) to be transversally stable comes from (53) with $j = 2$:

$$\kappa > \kappa_{in} = \frac{\alpha\beta\gamma\Lambda}{2(1+\beta\Lambda)}\;\frac{1}{\sin^2\left(\frac{\pi}{2M}\right)}\,. \tag{54}$$

For $K = 1$, inequality (53) is always satisfied and the necessary and sufficient condition for (46) to be transversally stable comes from (52) with $j = M$:

$$\kappa < \kappa_{anti} = \frac{1+\beta\Lambda}{4\alpha}\;\frac{1}{\cos^2\left(\frac{\pi}{2M}\right)}\,. \tag{55}$$

5.3. Summary of Analytical Results

We have shown that complete intensity synchronisation (16) is represented by solutions to (5) in the form of rotationally symmetric limit cycles (14) or (46). In-phase synchronisation (34) where all lasers oscillate in-phase requires (35)–(37), is given by

$$\begin{aligned} E_1(t) &= E_2(t) = \cdots = E_M(t) = \sqrt{\Lambda}e^{i(-\Delta_{out}+\kappa)t}, \\ N_1(t) &= N_2(t) = \cdots = N_M(t) = 0, \end{aligned} \tag{56}$$

and is stable if and only if the parameters satisfy (54). Anti-phase synchronisation (38) where each laser oscillates in anti-phase with its nearest neighbour(s) requires (35)–(36) and (39), is given by

$$\begin{aligned} E_1(t) &= -E_2(t) = \cdots = (-1)^{M-1}E_M(t) = \sqrt{\Lambda}e^{i(-\Delta_{out}-\kappa)t}, \\ N_1(t) &= N_2(t) = \cdots = N_M(t) = 0, \end{aligned} \tag{57}$$

and is stable if and only if the parameters satisfy (55).

Shading in Fig. 3 indicates stability of these two synchronised solutions in the parameter plane of shear within an individual laser, α, and the coupling strength between different lasers, κ. For $\alpha = 0$, both synchronised solutions are stable for all κ independent of the number of lasers, M. However, this is no longer the case for $\alpha > 0$. There is a lower bound on κ for the in-phase solution such that it is stable for $\kappa > \kappa_{in}$, and an upper bound on κ for the anti-phase solution such that it is stable for $\kappa < \kappa_{anti}$. Furthermore, both stability regions shrink with increasing either α or M.

Numerical bifurcation diagrams for three coupled lasers were reported in Ref. [13, Fig. 3 and 4], where parameter regions with stable synchronisation (14) are shaded in green. The analytical results derived here give new insights into the strong effects of α on the shape and extent of the green-shaded synchronisation regions in Ref. [13, Fig. 3 and 4]. More precisely, κ_{in} in (54) gives the condition for the pitchfork bifurcation at $\kappa = \Delta_{in} - \Delta_{out} = \Delta$ where the in-phase synchronised solution destabilises, and κ_{anti} in (55) gives the condition for the Hopf bifurcation at $\kappa = \Delta_{out} - \Delta_{in} = -\Delta$ where the anti-phase synchronised solution destabilises.

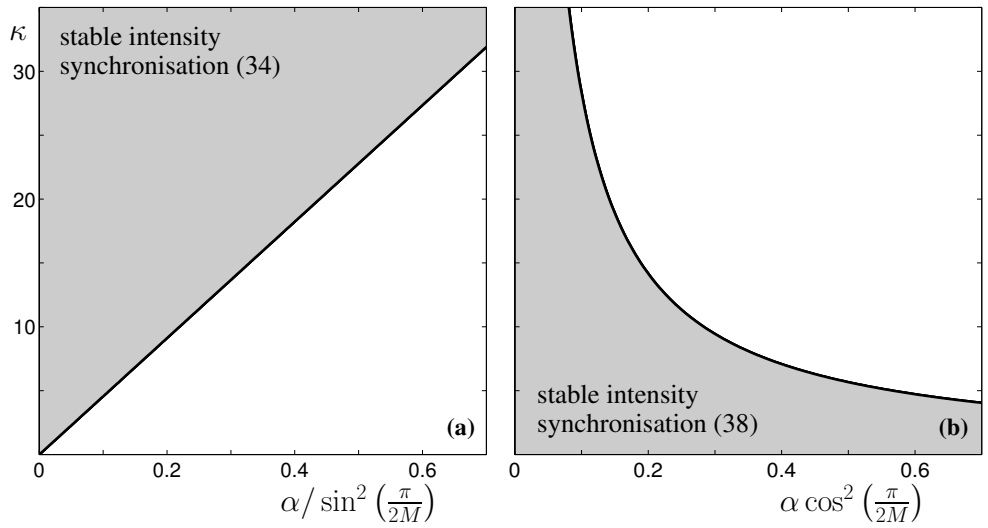

Figure 3: Shading indicates stability of (a) the in-phase solution (34) for $\Delta_{in} - \Delta_{out} = \kappa$, and (b) the anti-phase solution (38) for $\Delta_{in} - \Delta_{out} = -\kappa$.

6. Transitions from Complete Synchronisation to Optical Turbulence

Here we investigate transitions between complete synchronisation in the form of locking (14), and *optical turbulence* which we define as a chaotic attractor for (5) such that no lasers are synchronised. We consider $\mathbb{Z}_2$-symmetric arrays with identical outer lasers, $\Delta_1 = \Delta_M = \Delta_{out}$, and identical inner lasers, $\Delta_j = \Delta_{in}$ for $j = 2, \cdots, M-1$, and focus on the relevant transitions in the (κ, Δ) parameter plane, where $\Delta = \Delta_{in} - \Delta_{out}$. The analysis is performed in three steps. In the first step, we quantify the degree of synchronisation defined by

$$D(A) = \frac{2(M-2)!}{M!} \sum_{j=1}^{M-1} \sum_{j'=j}^{M} I(j, j') \,, \tag{58}$$

for an attractor A, where $I(j, j') = 1$ if lasers j and j' are synchronised (9)–(10) and 0 otherwise. $D = 1$ indicates complete synchronisation, $0 < D < 1$ indicates partial synchronisation, and $D = 0$ indicates that there is no synchronisation. In the second step, Lyapunov exponent calculations reveal different attractor types, and determine transverse stability of the corresponding synchronisation manifolds. In the third step, we conduct bifurcation analysis to identify the underlying mechanisms responsible for transitions between different types of synchronisation and for the complete loss of synchrony. To facilitate bifurcation analysis we use the $\mathbb{S}^1$-reduced system, obtained by rewritting (5) in magnitude and phase difference coordinates, so that synchronised solutions (14) can be studied as isolated equilibria. Henceforth, we refer to attractors of the $\mathbb{S}^1$-reduced system. We first analyse an array of three lasers and then study larger arrays.

Key	Synchronisation Type	Quantified by
CS	complete	$D = 1$
PS	partial	$1 > D > 0$
NS	none	$D = 0$
OT	none (optical turbulence)	$D = 0$ and $\mu_1 > 0$

Table 3: Colour online. Labelling/colour coding for optical turbulence and different degrees of synchronisation D defined in Eqn. (58). μ_1 denotes the largest Lyapunov exponent.

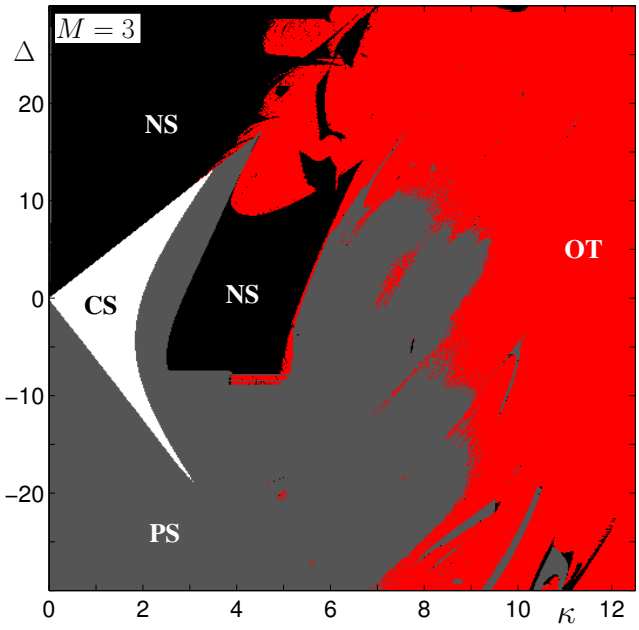

Figure 4: Colour online. The (κ, Δ) parameter plane for $\alpha = 2$ partitioned into regions of complete synchronisation (CS/white), partial synchronisation (PS/grey), and no synchronisation (NS/black and OT/red). OT/red indicates optical turbulence where the lasers are chaotic and not synchronised.

6.1. An Array of Three Coupled Laser Oscillators

Figure 4 shows regions of complete synchronisation (CS/white), partial synchronisation (PS/grey), and no synchronisation (NS/black and OT/red) [2]. Regions of optical turbulence (OT/red) are where no lasers are synchronised and the corresponding attractor has at least one positive Lyapunov exponent.

The Lyapunov diagram in Fig. 5(a) gives an overview of the different attractor types in the (κ, Δ) parameter plane. For small κ the plane is dominated by equilibria (EQ/green) and limit cycles (LC/grey). There are also small regions of tori (TR/blue). Towards increasing κ

[2]The (κ, Δ) plane is discretised into a grid of 800×800 points. For each fixed value of Δ we sweep κ using a (slightly perturbed) final point of the trajectory as an initial condition for the subsequent value of κ. For the calculations we use the coupled-laser model (5) to avoid singularities in the vector field of the $\mathbb{S}^1$-reduced system when $|E_j| = 0$.

Key	Attractor type/Bifurcation
EQ	equilibrium ⇒ phase-locking
LC	limit cycle (weakly - strongly attracting)
TR	torus (weakly - strongly attracting)
CH	chaotic attractor (slow - fast divergence)
	Fig. 5(b): attractor not in Fix($\mathbb{Z}_2$)
	Figs. 5(d) and 10(b)&(d): stable within Fix($\mathbb{Z}_2$) but transversally unstable
P	pitchfork bifurcation
H	Hopf bifurcation
SL	saddle-node of limit cycle bifurcation
PL	pitchfork of limit cycle bifurcation
T	torus (Neimark–Sacker) bifurcation
het	heteroclinic (relative homoclinic) bifurcation
PSL •	pitchfork-saddle-node of limit cycle bifurcation
PH •	pitchfork-Hopf bifurcation
HH •	Hopf–Hopf bifurcation
PT •	pitchfork-torus bifurcation
ShH •	relative Shilnikov bifurcation

Table 4: Colour online. Labelling and colour coding for different attractor types and bifurcations of system (5) with the $\mathbb{S}^1$ symmetry removed.

the system undergoes various bifurcations so that for $\kappa > 5$ the parameter plane is dominated by chaotic attractors (CH/yellow-red). The bifurcations that make up the stability boundary of equilibria have been studied in detail in [13]. Here, we focus on bifurcations making up the boundary of no synchrony in Fig. 4.

In Fig. 5(b) we shaded the regions of Fig. 5(a) if the corresponding attractor is not contained in the fixed-point subspace, Fix($\mathbb{Z}_2$). The key result is that non-shaded regions are the same as the combined regions of complete and partial synchronisation in Fig. 4, meaning that Fix($\mathbb{Z}_2$) is the synchronisation manifold associated with the regions of complete and partial synchronisation. The region of complete synchronisation in Fig. 4 is due to a stable equilibrium within Fix($\mathbb{Z}_2$), meaning that all three lasers have constant intensities. The outer two lasers have equal intensities and phases (intensity and in-phase synchronisation). The middle laser has different intensity and is out-of-phase with the outer lasers except for the two special cases, $\Delta_{in} - \Delta_{out} = \pm\kappa$, studied analytically in § 5.2. The regions of partial synchronisation in Fig. 4 comprise periodic, quasi-periodic, and chaotic intensity oscillations. There, only the outer two lasers are synchronised, and they have equal intensities and phases (intensity and in-phase synchronisation).

Shaded region boundaries in Fig. 5(b) relate to synchronisation boundaries. *Genuine* synchronisation boundaries coincide with bifurcations and are responsible for transitions between attractors within and off the fixed-point subspace. What is more, they can be classified into two types: 'smooth' and 'rough'. In addition to genuine boundaries, there are also *artificial* boundaries. These depend on the choice of path in the parameter plane, do

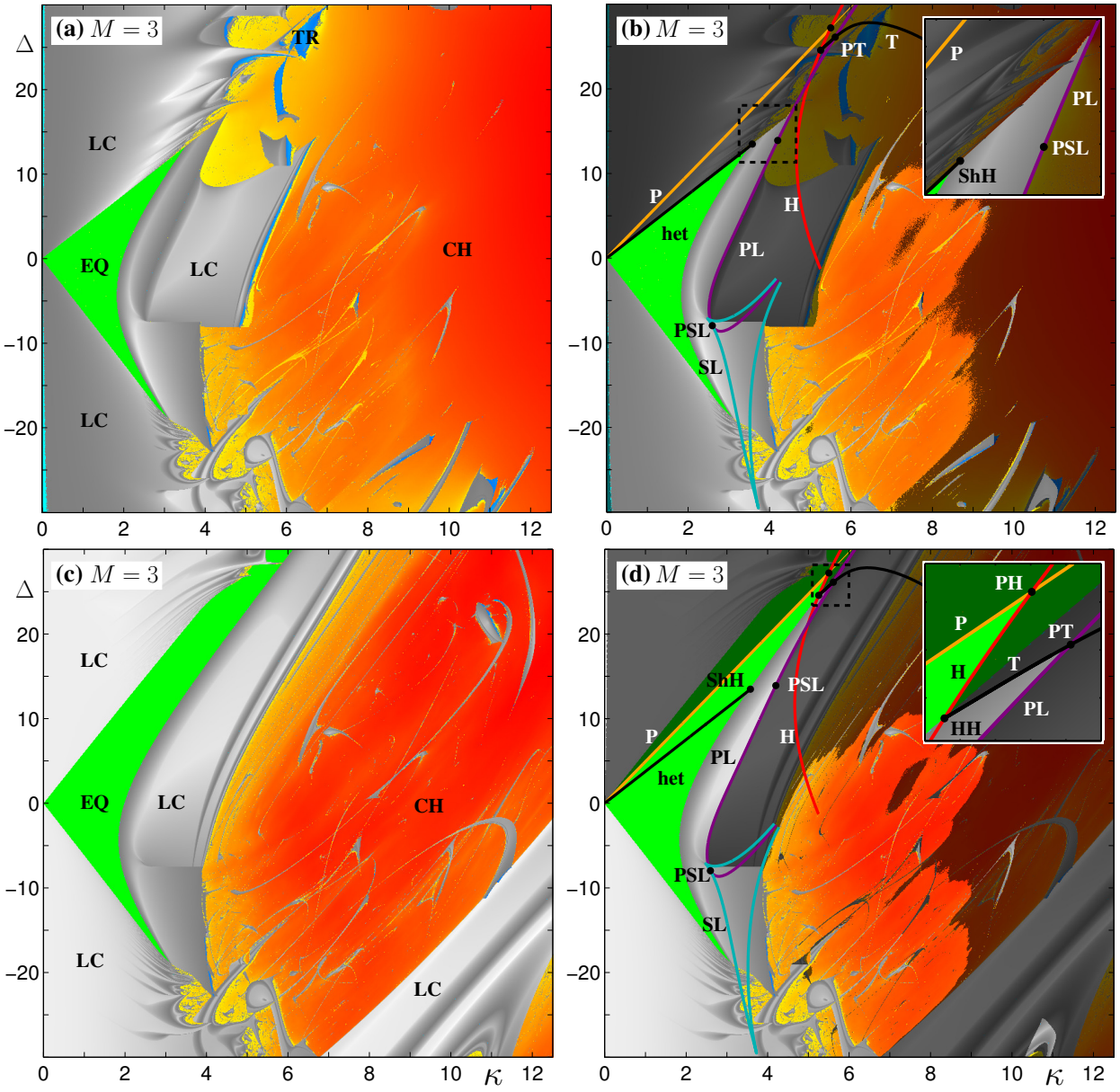

Figure 5: Colour online. Two-parameter stability diagrams in the (κ, Δ) plane for $\alpha = 2$. (a) Attractors of the $\mathbb{S}^1$-reduced system. (b) Regions of (a) are shaded if the corresponding attractor is not in the fixed-point subspace $\mathrm{Fix}(\mathbb{Z}_2)$. (c) Attractors of the $\mathbb{S}^1$-reduced system restricted to $\mathrm{Fix}(\mathbb{Z}_2)$. (d) Regions of (c) are shaded if the corresponding attractor is transversally unstable. Also included in (b) and (d) are the key bifurcation curves. For the labelling and colour coding see Table 4.

not coincide with any bifurcation curves, but are related to bistability.

6.1.1. Bifurcations of Non-Chaotic Attractors

Starting from the origin and moving clockwise we identify different bifurcations associated with genuine synchronisation boundaries. Along the curve of heteroclinic bifurcations

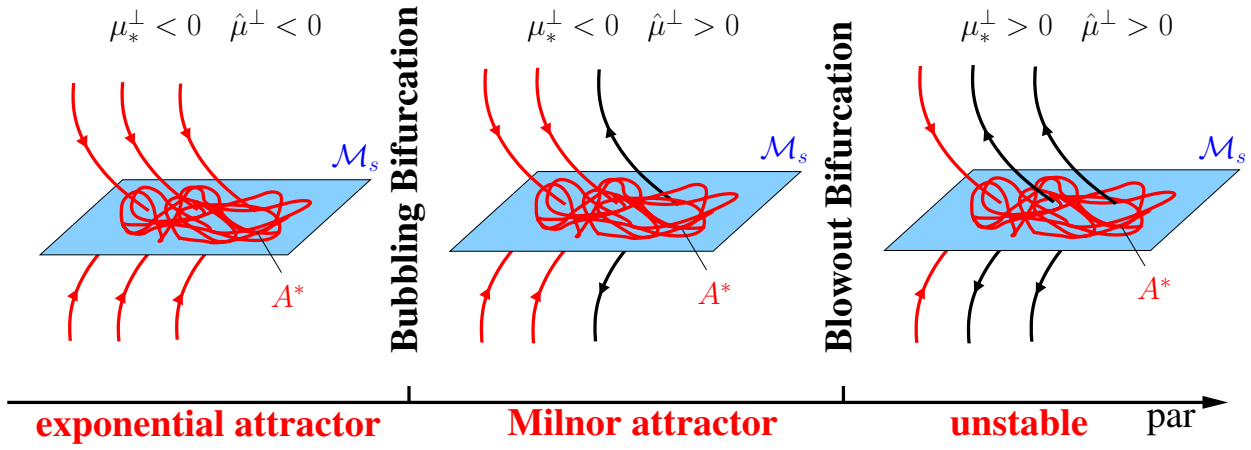

Figure 6: Colour online. A schematic showing changes in dynamics as the system passes through a blowout bifurcation. The (grey/blue) plane is an invariant synchronisation manifold containing a chaotic attractor A^*, and the lines represent the stable and unstable manifolds of periodic orbits embedded in A^*.

(het) that emerges from the origin and ends at the Shilnikov–Hopf bifurcation (ShH), a symmetric [45, Ch. 7.4] limit cycle not within the synchronisation manifold $\mathrm{Fix}(\mathbb{Z}_2)$ is destroyed as it collides with two symmetrically related saddle equilibria to form a (non-robust) heteroclinic cycle. For (κ, Δ) below het, the system settles down to a stable equilibrium (complete synchrony). At the Shilnikov–Hopf bifurcation [46] both saddle equilibria involved in the heteroclinic cycle simultaneously undergo a Hopf bifurcation. It is thought that additional bifurcations emerging from ShH form the boundary connecting ShH and the curve of pitchfork of limit cycle bifurcations (PL) (see the inset). The next part of the boundary is formed by PL. Along the subcritical part of PL, between the pitchfork-torus bifurcation (PT) and the first pitchfork-saddle-node bifurcation (PSL), a stable limit cycle contained in the fixed-point subspace collides with two unstable limit cycles and turns unstable. The chaotic region to the right of the subcritical part of PL involves intermittent chaos [47, Ch. 8.2] not in the fixed-point subspace. Along the supercritical part of PL, between the two PSL points, a stable limit cycle contained in the fixed-point subspace loses stability and two stable limit cycles bifurcate out of the fixed-point subspace. The region in Fig. 5(a)–(b), to the right of the supercritical part of PL, corresponds to one of these two stable limit cycles. This is the last 'smooth' part of the genuine synchronisation boundary. The horizontal boundary to the right of the lower PSL is an artificial boundary due to bistability. The remaining genuine boundary is 'rough'. Since it corresponds to bifurcations of chaotic attractors, this boundary cannot be analysed using existing bifurcation continuation methods [48]. Instead, one needs to calculate Lyapunov exponents in directions tangent and transverse to the synchronisation manifold $\mathrm{Fix}(\mathbb{Z}_2)$, as described in the Appendix. We first give a short description of tangential and transverse Lyapunov exponent diagrams and then explain the 'rough' synchronisation boundary.

In Fig. 5(c) tangential Lyapunov exponents have been used to indicate different attractor types (see Table 4) of the $\mathbb{S}^1$-reduced system restricted to $\mathrm{Fix}(\mathbb{Z}_2)$. In Fig. 5(d) regions of

the (κ, Δ) plane are shaded if the attractor within synchronisation manifold $\mathrm{Fix}(\mathbb{Z}_2)$ has at least one positive transverse Lyapunov exponent, meaning that it is unstable in the full system. Notice that the non-shaded region in Fig. 5(d) is larger than in Fig. 5(b) indicating bistability between attractors within and off the synchronisation manifold $\mathrm{Fix}(\mathbb{Z}_2)$.

As in Fig. 5(b), boundaries of the shaded regions in Fig. 5(d) are of two types: genuine synchronisation boundaries that do coincide with bifurcations, and artificial boundaries that do not. Starting from the origin and moving clockwise, the genuine synchronisation boundaries are formed by the curves of pitchfork (P), Hopf (H), torus (T) and pitchfork of limit cycle (PL) bifurcations shown in Fig. 5(d). Along the subcritical pitchfork bifurcation P, between the origin and the pitchfork–Hopf point (PH), a stable equilibrium in the fixed-point subspace loses stability as it collides with two unstable equilibria not in the fixed-point subspace. Along the supercritical Hopf bifurcation, between PH and the Hopf–Hopf point (HH), a stable equilibrium in the fixed-point subspace bifurcates to a limit cycle off the fixed-point subspace and loses transverse stability. Emanating from HH is a curve of torus bifurcations (T) which marks the boundary between HH and the pitchfork-torus point (PT). Along this part of T, a stable limit cycle within the fixed-point subspace loses transverse stability in a subcritical torus bifurcation. The remaining 'smooth' genuine boundary consists of PL described in the previous paragraph.

6.1.2. Bifurcations of Chaotic Attractors along the 'rough' synchronisation boundaries.

The largest transverse Lyapunov exponent, $\mu_*^\perp$, approximates the average rate of exponential growth/decay in a direction transverse to the synchronisation manifold $\mathrm{Fix}(\mathbb{Z}_2)$, for typical initial conditions on a chaotic attractor A^* for the $\mathbb{Z}_2$-restricted system. The 'rough' boundaries of shaded regions in Fig. 5(d) correspond to *blowout bifurcations* where $\mu_*^\perp$ crosses through zero and A^* loses stability transverse to $\mathrm{Fix}(\mathbb{Z}_2)$. To describe the interesting dynamical phenomena that take place near blowout bifurcations we also need to consider $\hat{\mu}^\perp = \max_{\mathbf{x}_0 \in A} \mu^\perp(\mathbf{x}_0)$ [47, Ch. 10], where $\mu^\perp$ is the largest transverse Lyapunov exponent for any initial condition $\mathbf{x}_0$ on A^* (not just the typical ones). The set of initial conditions such that $\mu^\perp(\mathbf{x}_0) \neq \mu_*^\perp$, occupies zero volume of the synchronisation manifold $\mathrm{Fix}(\mathbb{Z}_2)$ and typically corresponds to unstable periodic orbits embedded in A^*. The sketch in Fig. 6 illustrates the relationship between $\mu_*^\perp$ and $\hat{\mu}^\perp$ as a parameter is varied across a blowout bifurcation. If $\hat{\mu}^\perp < 0$ then by definition $\mu_*^\perp < 0$, and A^* is an exponentially stable attractor for the full system. As a parameter is increased further, a periodic orbit embedded in A^* loses transverse stability and $\hat{\mu}^\perp$ crosses through zero in a *bubbling bifurcation* [49, 50]. Now every neighbourhood of A^* contains trajectories that at some point leave that neighbourhood. If the bubbling bifurcation is *supercritical* then those trajectories return and eventually converge to A^*. However, if it is *subcritical* then those trajectories never return to the neighbourhood of A^*. In either case, A^* is no longer an exponentially stable attractor, in fact it is not even Lyapunov stable. However, it is still a Milnor attractor [51, 52], meaning that its basin of attraction occupies a positive volume of the phase space. On increasing a parameter further, more and more periodic orbits embedded in A^* lose transverse stability causing $\mu_*^\perp$ to cross through zero in a blowout bifurcation. Past this bifurcation, the basin of attraction of A^* takes up zero volume of the phase space and A^* is not even a Milnor

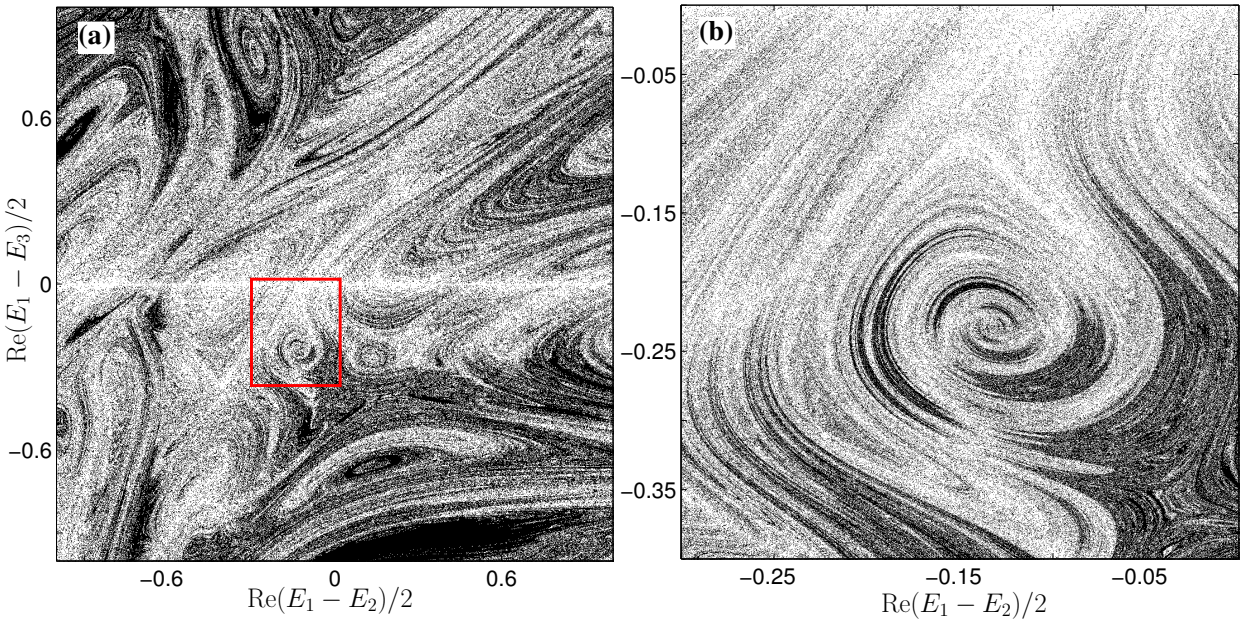

Figure 7: Colour online. Riddled basin of attraction for $(\alpha, \kappa, \Delta) = (2, 5.642, 6.44)$. White points indicate initial conditions that converge to the chaotic attractor within the fixed-point subspace at $\mathrm{Re}(E_1 - E_3)/2 = 0$, and black points denote initial conditions that do not. (b) An expanded view indicated by the box in (a).

attractor. If the bubbling and blowout bifurcations are supercritical then there is a new, larger attractor A that intersects $\mathrm{Fix}(\mathbb{Z}_2)$ and contains A^* [53].

Bubbling bifurcation and its criticality. In general it is difficult to calculate the parameter values for which bubbling bifurcations occur. The exact periodic orbits that lose transverse stability are unknown and could even change in a non-trivial fashion as parameters vary—Hunt and Ott [54] conjectured that they are periodic orbits with a low period. Nonetheless, one can observe different effects of a bubbling bifurcation depending on its criticality. We illustrate the two different cases by starting from a point in A^*, applying a perturbation, and studying the resulting trajectory. In the supercitical case we only perturb a very small amount in the transverse direction, $\mathrm{Re}(E_1 - E_3)/2 \sim 10^{-6}$. Between the bubbling and blowout bifurcations, the resulting trajectory makes a number of large excursions away from the synchronisation manifold $\mathrm{Fix}(\mathbb{Z}_2)$ but eventually converges back to A^* (not shown). The subcritical case of the bubbling bifurcation results in A^* having a *riddled basin of attraction* [55]. In between the bubbling and blowout bifurcations, any neighbourhood of an initial condition belonging to the basin of attraction of A^* will contain a positive volume of phase space that belongs to the basin of attraction of a different attractor. Figure 7 contains a two-dimensional slice of a riddled basin in the three coupled laser model for parameter values close to blowout bifurcation, $(\alpha, \kappa, \Delta) = (2, 5.642, 6.44)$. In Fig. 7, each point in the $(\mathrm{Re}(E_1 - E_2)/2, \mathrm{Re}(E_1 - E_3)/2)$ plane represents one perturbation; the points are coloured white if the resulting trajectory converges to A^*, or black if it converges to a different attractor. Since A^* is still an asymptotically stable attractor for the restriction

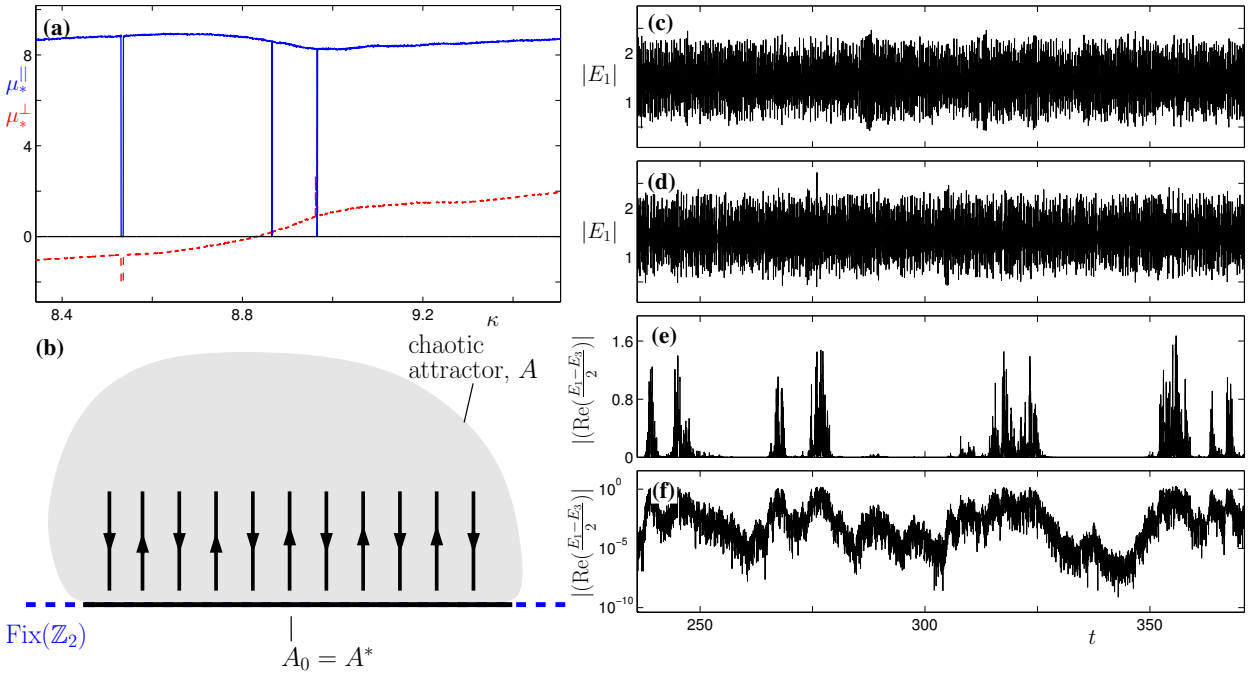

Figure 8: Colour online. (a) Largest tangential (solid blue line) and transverse (dashed red line) Lyapunov exponents for a parameter sweep in κ. (b) A sketch illustrating on-off intermittency due to repulsion from and attraction towards the *same* chaotic attractor, A^*, for the $\mathbb{Z}_2$-restricted system. (c)–(f) Time series indicating on-off intermittency in the three coupled-laser model. (c) Chaotic attractor for the $\mathbb{Z}_2$-restricted system. (d) On-off intermittent chaotic attractor for the full system. (e)–(f) Dynamics in the direction transverse to Fix($\mathbb{Z}_2$) plotted on a (e) linear and (f) logarithmic scale. $(\alpha, \kappa, \Delta) = (2, 8.89, 0)$.

of the full system to Fix($\mathbb{Z}_2$), any perturbation solely within the synchronisation manifold Fix($\mathbb{Z}_2$) converges to A^* and hence there is a white line at $\mathrm{Re}(E_1 - E_3)/2 = 0$ in Fig. 7(a).

Blowout bifurcation and on-off or in-out intermittency. Past the blowout bifurcation, one expects intermittent dynamics on the new attractor A that intersects Fix($\mathbb{Z}_2$). To facilitate the discussion, it is useful to define $A_0 = A \cap \mathrm{Fix}(\mathbb{Z}_2)$; note that A_0 and $A \cap \mathrm{Fix}(\mathbb{Z}_2)^C$ (where ^{C} denotes the complement) are both non-empty. Furthermore, if A is an asymptotic attractor then A_0 must contain a Milnor attractor for the $\mathbb{Z}_2$-restricted system [56], which we denote by A^*.

If $A^* = A_0$, then the attractor A for the full system displays *on-off intermittency*. Figure 8(b) contains a sketch illustrating the fact that repelling and attracting sets responsible for on-off intermittency are intermingled in A_0. In Fig. 8(c)–(f) we show an example believed to be on-off intermittency in the three coupled laser model. The time series for the chaotic attractor A_0 of the $\mathbb{Z}_2$-restricted system (Fig. 8(c)) is similar to that of the on-off intermittent attractor A of the full system (Fig. 8(d)). Intermittent behaviour shows up as bursting away from A_0 (Fig. 8(e)). The same figure with the y-axis plotted on a logarithmic scale (Fig. 8(f)) shows no evidence of distinctively different mechanisms responsible for repulsion away from and attraction towards A_0. This observation is in line with the sketch in Fig. 8(b).

If $A^* \subset A_0$, then A displays *in-out* intermittency. For in-out intermittency different

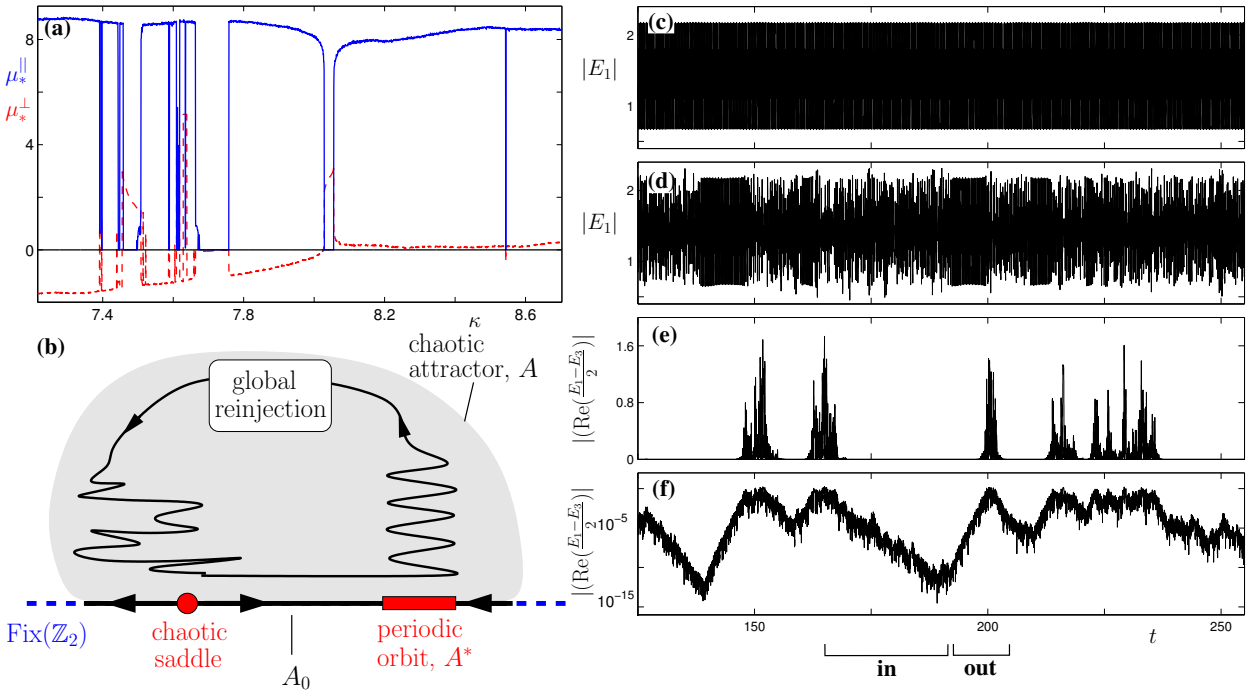

Figure 9: Colour online. (a) Largest tangential (solid blue line) and transverse (dashed red line) Lyapunov exponents for a parameter sweep in κ. (b) A sketch illustrating in-out intermittency organised by *different* invariant sets (red) within the invariant synchronisation manifold Fix($\mathbb{Z}_2$) (blue dashed). (c)–(f) Time series indicating in-out intermittency in the three coupled-laser model. (c) Stable limit cycle for the $\mathbb{Z}_2$-restricted system. (d) In-out intermittent chaotic attractor for the full system. (e)–(f) Dynamics in the direction transverse to Fix($\mathbb{Z}_2$) plotted on a (e) linear and (f) logarithmic scale. $(\alpha, \kappa, \Delta) = (2, 8.046875, -6)$.

mechanisms are responsible for the repulsion away from and attraction towards A_0. Figure 9(b) shows a sketch with one attractive and one repulsive mechanism. A trajectory on the attractor A of the full system is repelled from A_0 along the unstable manifold of a limit cycle that is contained in A_0 and is stable to perturbations within Fix($\mathbb{Z}_2$)—this is the *out phase*. The trajectory is then globally reinjected towards A_0, and the *in phase* begins when it approaches A_0 along a stable manifold of a chaotic saddle contained in A_0. The chaotic saddle is repelling within Fix($\mathbb{Z}_2$), meaning that the trajectory will eventually approach the limit cycle again, then move away from A_0, and so on. In Fig. 9(c)–(f) we show an example of in-out intermittency in the three-coupled laser model. On the one hand, transverse and tangential Lyapunov exponents in Fig. 9(a) along with the time series in Fig. 9(c) confirm that there exists a limit cycle that is unstable for the full system but stable within Fix($\mathbb{Z}_2$). During the intermittent (bursting) dynamics (Fig. 9(d)–(e)), this limit cycle is clearly visible in the time series for the attractor of the full system (Fig. 9(d)). What is more, 'spells' of periodic-like oscillations due to this limit cycle coincide with *out phases* during which the system is repelled from A_0 (Fig. 9(d)–(f)). On the other hand, it is clear from Fig. 9(d)–(f) that quite different mechanism(s) are responsible for attraction towards A_0. A diffusive character of the time series during the *in phase* indicated in Fig. 9(f) strongly suggest the

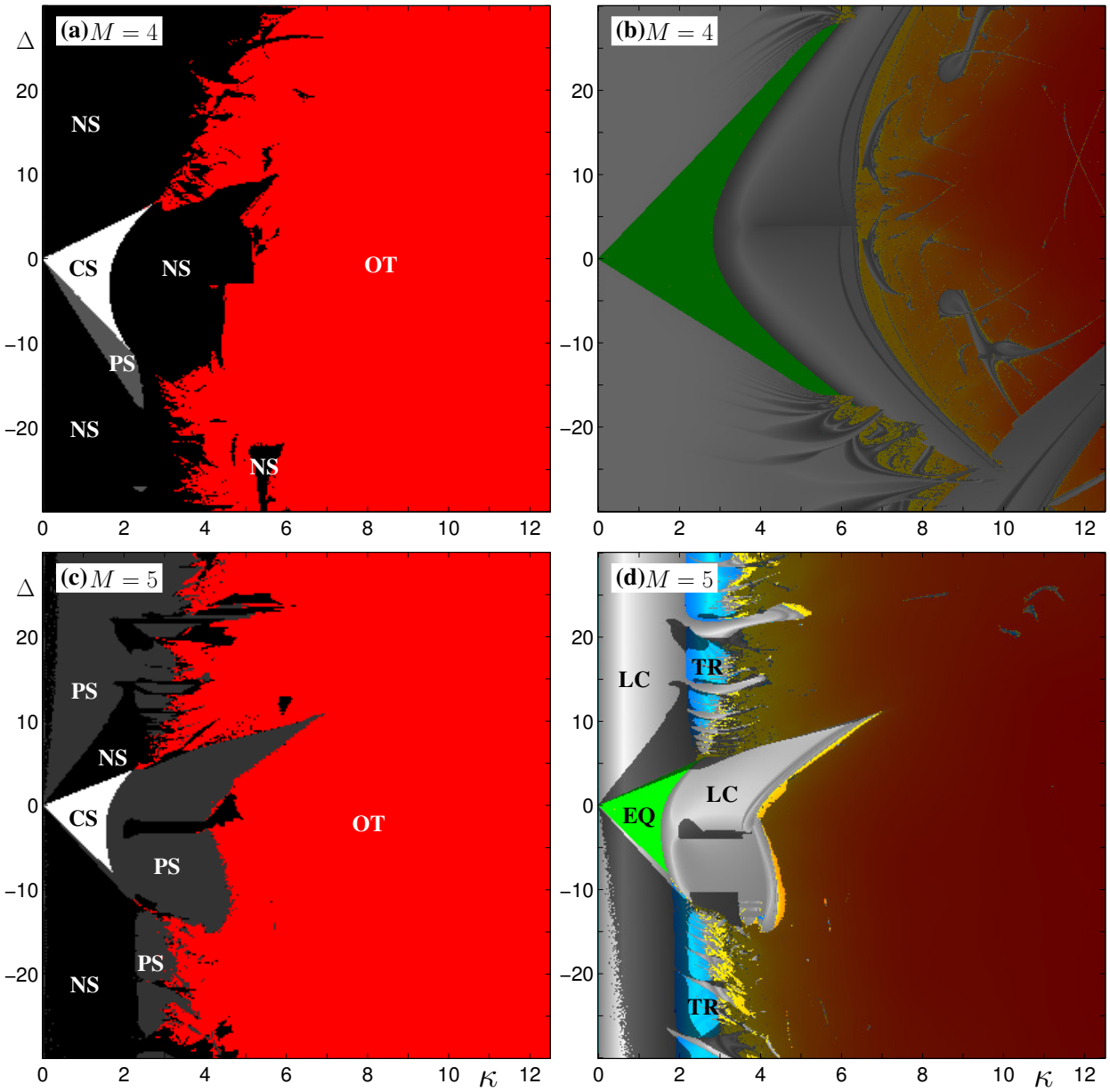

Figure 10: Colour online. The (κ, Δ) plane with $\alpha = 2$ for (top) $M = 4$ and (bottom) $M = 5$ partitioned into regions of (a and c) different degree of synchronisation and optical turbulence, and (b and d) different attractor types quantified by the (colours) tangential and (shading) transverse Lyapunov exponents for Fix($\mathbb{Z}_2$). For colour coding and labelling see Tables 3 and 4.

influence of a chaotic saddle. While the *in* and *out* phases indicated in the mid-part of the time series are in line with the sketch in Fig. 9(a), there appear to be other attracting mechanisms visible at the beginning and end of that time series. This suggest a possibility of *generalised* in-out intermittency in which there are many forms of 'in'-dynamics and/or many forms of 'out'-dynamics [57].

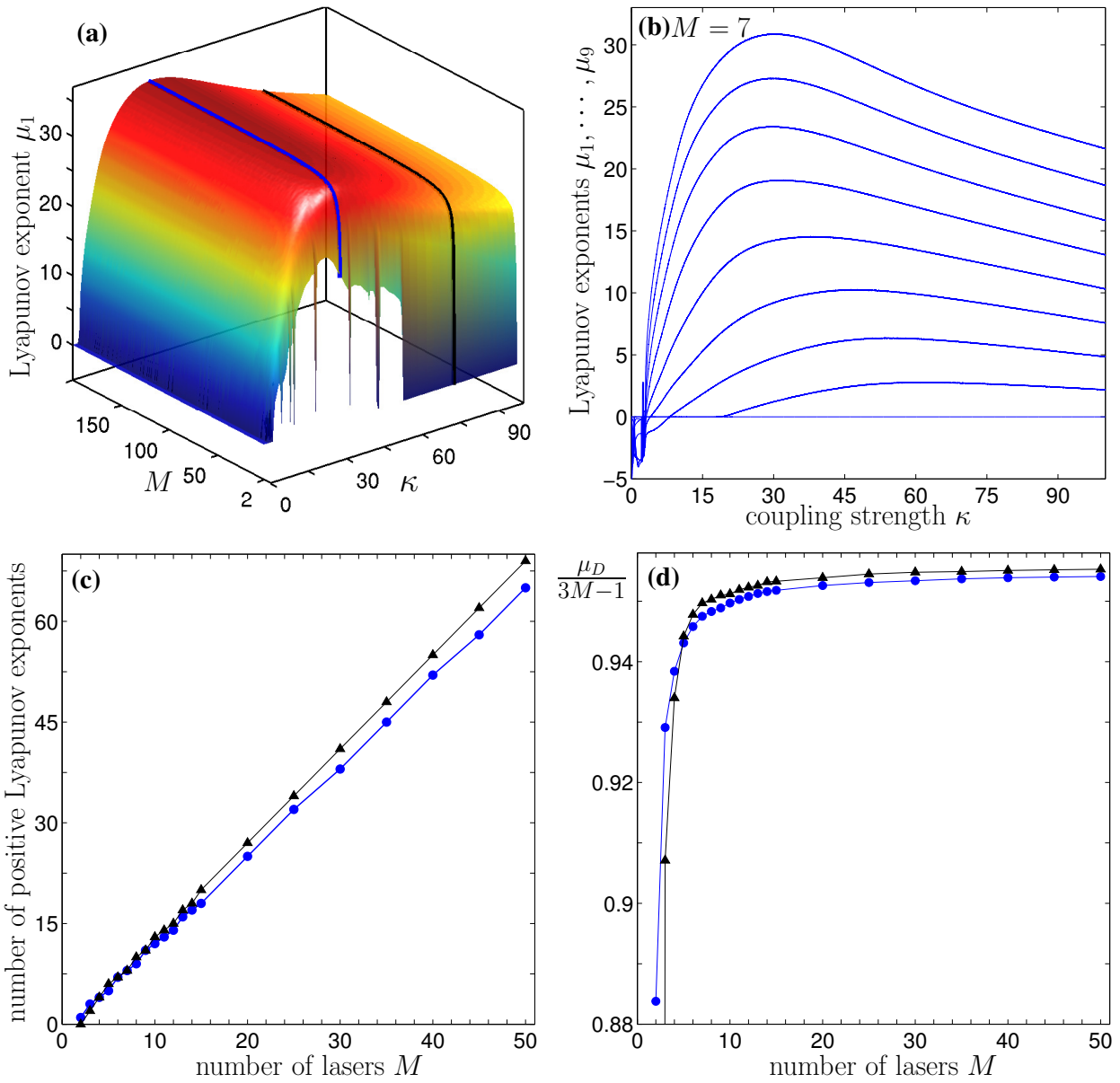

Figure 11: Colour online. (a) Dependence of the largest Lyapunov exponent, μ_1, on array size M and coupling strength κ. (b) Dependence of the nine largest Lyapunov exponents on κ for an array with $M = 7$. (c) Number of positive Lyapunov exponents and (d) normalised Lyapunov dimension as functions of M for $\kappa = 30$ (•) and $\kappa = 75$ (▲). $(\alpha, \Delta) = (5, 0)$.

6.2. Larger Arrays of Coupled Laser Oscillators

For larger laser arrays there are more possible synchronisation manifolds corresponding to different types and degrees of intensity synchronisation. An interesting question arises: is the fixed-point subspace Fix($\mathbb{Z}_2$) still a stable synchronisation manifold? To answer this question we partitioned the (κ, Δ) plane into regions with different degree of synchronisation

using (58), different attractor types within $\mathrm{Fix}(\mathbb{Z}_2)$ and their transverse stability. In this way, we analysed system (5) with $M = 4, 5, 6$ and 7, and identified recurring patterns that are illustrated in Fig. 10 for $M = 4$ and $M = 5$.

In all cases that we considered, the (κ, Δ) plane features one region of complete synchronisation (stable equilibria) which is confined to small κ and centred around $\Delta = 0$, only one degree of partial synchronisation, and vast regions of optical turbulence. We spotted two main differences between laser arrays with M odd and even. Firstly, the proportion of the (κ, Δ) plane with an attractor corresponding to partial synchronisation is significantly smaller for M even. Secondly, the relationship between partially synchronised lasers is different. For arrays with an even number of lasers, $M = 2L$, we did not find any attractors contained in $\mathrm{Fix}(\mathbb{Z}_2)$ (see Fig. 10(b)). Rather, the regions of complete and partial synchronisation are due to attractors contained in the synchronisation manifold given by

$$\begin{aligned} E_1 = -E_{2L}\,, \quad E_2 = -E_{2L-1}\,, \quad \cdots \quad E_L = -E_{L+1}\,, \\ N_1 = N_{2L}\,, \quad N_2 = N_{2L-1}\,, \quad \cdots \quad N_L = N_{L+1}\,, \end{aligned}$$

meaning that the laser pairs with the same shading/colour in Table 2 are intensity synchronised in anti-phase. In contrast to this, for M odd, regions of complete and partial synchronisation correspond to attractors contained in $\mathrm{Fix}(\mathbb{Z}_2)$, meaning that the laser pairs are intensity synchronised in-phase. Finally, note that for $M \geq 5$ and odd, there are only small parameter regions with partially synchronised chaos (see Fig. 10(c)–(d)).

7. Properties of Optical Turbulence

For α sufficiently large, the (κ, Δ) parameter plane is dominated by optical turbulence. This section studies properties of the underlying chaotic attractors based on $3M-1$ Lyapunov exponents, $\mu_1 \geq \mu_2 \geq \cdots \geq \mu_{3M-1}$, for the reduced system without $\mathbb{S}^1$ symmetry. The intensity of the chaos [58] is quantified by μ_1, the number of unstable directions is given by the number of positive Lyapunov exponents, and the fraction of phase space that the chaotic attractor explores is given by the Lyapunov dimension [59]:

$$\mu_D = I + \frac{\sum_{i=1}^{I} \mu_i}{|\mu_{i+1}|}\,, \tag{59}$$

where I is the highest integer such that $\sum_{i=1}^{I} \mu_i > 0$. When studying the dependence of the Lyapunov dimension on array size, it is useful to look at *normalised* Lyapunov dimension, $\mu_D/(3M-1)$, expressed as a percentage of the total phase space. For the following analysis we set $\alpha = 5$ since it is known that large α is conducive to the creation of chaos [60, 61]. The results do not vary much over the considered range of $|\Delta| < 30$, so we present here the case of identical lasers given by $\Delta = 0$.

Figure 11(a), shows the dependence of μ_1 on the number of lasers, M, and the coupling strength, κ. For $M \geq 4$, μ_1 increases rapidly above zero, reaches a maximum around $\kappa \approx 30$, and then gradually decreases. Fixing κ and increasing M results in μ_1 converging

to a κ-dependent constant. We would like to point out that periodic windows within chaos, indicated by μ_1 dropping to zero, were observed only for $M = 2$ and 3. No periodic windows were detected for $M \geq 4$ despite having 10^4 points within the plotted interval of κ. This result suggest that, from a practical point of view, unsynchronised chaos generated by (semiconductor) laser arrays is persistent under parameter changes.

Figure 11(b) shows that for $M = 7$ there are at most eight positive Lyapunov exponents. Figures 11(c) and (d) explore the dependence of the number of positive Lyapunov exponents on array size in more extent for two values of the coupling strength, namely $\kappa = 30$ (●) and $\kappa = 75$ (▲); these values of κ are also indicated by blue ($\kappa = 30$) and black ($\kappa = 75$) curves in Fig. 11(a). For each value of κ we calculate the Lyapunov spectrum with increasing array size, M, and plot the number of positive Lyapunov exponents in Fig. 11(c) and the normalised Lyapunov dimension in Fig. 11(d). On the one hand, the number of positive Lyapunov exponents increases monotonically with M. On the other hand, the normalised Lyapunov dimension increases rapidly at first, but then saturates at $\approx 95.4\%$ for $\kappa = 30$, and at ≈ 95.5 % for $\kappa = 75$.

From these observations we conclude that the chaos intensity characterised by μ_1, as well as the normalised Lyapunov dimension characterised by $\mu_D/(3M - 1)$, both saturate to a constant value for relatively small array size ($M \approx 15$). Recently, a different behaviour has been observed for globally coupled phase oscillators, where chaos intensity was maximised by an optimal oscillator number (M=10) above which μ_1 decreases [58]. In view of these findings, our results highlight potential differences between chaotic behaviour of nearest-neighbour and globally coupled oscillators. Furthermore, the dependence of the Lyapunov spectrum on κ and M reported here shows good qualitative agreement with results in Refs. [62, 63]. Those papers studied persistent chaos in high dimensional dynamical systems and conjectured that, as the dimension of a typical dissipative dynamical system is increased, the number of positive Lyapunov exponents increases monotonically and the number of windows with periodic behaviour decreases. It was also conjectured that at large coupling all the Lyapunov exponents become negative again. In the M coupled laser model (5) this occurs for (unrealistically) large κ not shown in the figures.

8. Conclusion

This paper combined analytical and numerical techniques from (equivariant) bifurcation theory to provide a comprehensive study of various (periodic, chaotic, complete, partial) synchronisation types, as well as synchronisation-desynchronisation transitions, in a linear array of M coupled laser oscillators (Fig. 1). Synchronisation was defined in (9)–(10) as a fixed-in-time relationship between properties of light emitted by individual lasers. The lasers were modelled by class-B rate equations and assumed to be identical with the exception of different natural frequencies. Particular focus was placed on a parametric study with dependence on the coupling strength, laser frequency detuning, amount of shear or amplitude-phase coupling in a single laser, and the array size M.

Firstly, we classified and gave analytical conditions for the existence and stability of complete intensity synchronised solutions, where all lasers have the same frequency and

intensity. We showed that such solutions require frequency detunings between certain lasers. Depending on the allowed combinations of the detunings, complete intensity synchronisation can arise in arrays that are reflectionally symmetric but also in those that are not. Each allowed combination of frequency detunings determines which lasers emit in-phase or in anti-phase with each other. We studied stability of two special cases where: (i) all the lasers emit in-phase and (ii) each laser emits in anti-phase with its neighbour(s). In the absence of shear, both solutions are stable for all coupling strengths, independent of the array size. However, in the presence of shear, the in-phase solution is only stable above some critical value of the coupling strength, κ_{in} (54), and the anti-phase solution is only stable below some critical value of the coupling strength, κ_{anti} (55). In addition to these two special cases, there are $2^{M-1} - 2$ other complete intensity synchronised solutions that warrant further stability analysis. These analytical findings provided new insights into numerical bifurcation diagrams for coupled lasers found in the literature.

Secondly, through a combination of numerical bifurcation analysis and Lyapunov exponent calculations, we studied transitions between different synchronisation types in the parameter plane of the coupling strength and frequency detuning between the outer two lasers and the inner laser(s). More specifically, we found: one region of constant-intensity complete synchronisation where the outer two lasers emit in-phase but typically out-of-phase with the inner laser(s); regions of partial synchronisation comprising of periodic, quasi-periodic and chaotic intensity oscillations; and vast regions of optical turbulence where no lasers are synchronised and each laser is chaotic. Synchronisation-desynchronisation transitions appeared as two types of boundaries in the parameter plane: 'smooth' and 'rough'. We identified bifurcations associated with different boundaries, and studied the 'rough' boundaries in more detail in terms of blowout bifurcations of chaotic attractors and the ensuing on-off or in-out intermittency. Detailed calculations for an array of three lasers were complemented by studying the effects of different array size. In particular, the analysis of invariant synchronisation manifolds revealed differences between synchronisation types found for an even and odd number of lasers. Furthermore, regions of synchronised chaos were found to shrink for larger arrays, where the parameter plane is dominated by optical turbulence.

Thirdly, we used the Lyapunov spectrum of underlying chaotic attractors to study properties of optical turbulence. We found that optical turbulence is persistent for $M > 3$, meaning that no periodic windows were detected within the prescribed numerical accuracy. Furthermore, the persistence and intensity of chaos increases rapidly and then remains nearly constant (saturates) with increasing array size. These results revealed differences from studies carried out on globally coupled phase oscillators [58], where chaos intensity is maximised by an optimal array size. Further research is needed to ascertain if this difference is due to the coupling structure (nearest-neighbour vs. global), the oscillator type (amplitude-and-phase vs. phase), or a combination of both.

Acknowledgements

NB would like to thank P. Ashwin and J. Dawes for their useful comments on intermittency. PD and SW were supported by the EPSRC grant EP/H019197/1.

Appendix A. Computation of Lyapunov Exponents

To compute Lyapunov exponents (LEs) we numerically integrate an extended system [64, 65, 66] which comprises the original system (5), and its linearisation that governs the time evolution of a perturbation vector, $\xi(t) = (\xi_1(t), \cdots, \xi_M(t))^T \in \mathbb{R}^{3M}$,

$$\frac{d\xi_j}{dt} = \mathbf{Df}_j(\mathbf{x}_j)\xi_j + \kappa \sum_{j'=1}^{M} G_{jj'}\mathbf{H}\xi_{j'}\,, \tag{A.1}$$

where $\mathbf{Df}_j(\mathbf{x}_j)$ is the Jacobian of (4) evaluated along a trajectory of the original system. Equations (5) and (A.1) are numerically integrated subject to initial conditions

$$(\mathbf{x}_1(0), \cdots, \mathbf{x}_M(0))^T \in A \quad \text{and} \quad \xi(0) = \mathbf{v}\,,$$

where A is an attractor of interest, and $\mathbf{v}$ has length one and points in an arbitrary direction. The vector $\xi(t)$ is renormalised to length one at times $t_k = k\,\tau$, where $k = 1, \cdots, n$. The largest LE of A is approximated by

$$\mu_1 = \frac{1}{n\tau}\sum_{k=1}^{n} \ln|\xi(t_k)|, \tag{A.2}$$

for suitably chosen n and τ, and using $\xi(t_k)$ before renormalisation. To compute the remaining LEs we need to know the evolution of $l = 2, \cdots, 3M$ vectors under (A.1). These vectors must be initially orthonormal, and are orthonormalised at times t_k using Gram-Schmidt orthonormalisation [65]. The remaining LEs are obtained from

$$\sum_{i=1}^{l} \mu_i = \frac{1}{n\tau}\sum_{k=1}^{n} \ln(V(l, t_k)), \tag{A.3}$$

where $V(l, t_k)$ is the l-dimensional volume of the phase-space spanned by the l vectors before orthonormalisation.

Appendix A.1. Tangential and Transverse Lyapunov Exponents for Attractors Within the Invariant Synchronisation Manifold Fix($\mathbb{Z}_2$)

The Lyapunov spectrum of an attractor contained in an invariant synchronisation manifold, such as Fix($\mathbb{Z}_2$), splits into two sets. Elements of the first set are known as *tangential LEs*, they correspond to perturbations solely within Fix($\mathbb{Z}_2$), and are denoted by $\mu_j^{\|}$. Elements of the second set are known as *transverse LEs*, they correspond to perturbations solely in a direction transverse to Fix($\mathbb{Z}_2$), and are denoted by $\mu_j^{\perp}$.

Appendix A.1.1. Tangential Lyapunov Exponents

To compute tangential LEs for $M = 2L-1$ odd and $M = 2L$ even, we numerically integrate two systems. The first system is the restriction of (5) to $\mathrm{Fix}(\mathbb{Z}_2)$. It is obtained by equating variables of lasers marked with the same shade/colour in the second column of Table 2, as illustrated in the third column of Table 2. The second system is the linearisation of the restricted system and governs the time evolution of the perturbation vector $\xi^{\parallel}(t) = (\xi_1^{\parallel}(t), \cdots, \xi_L^{\parallel}(t)) \in \mathrm{Fix}(\mathbb{Z}_2)$. The resulting sets of equations have the same general form as (5) and (A.1), but with $j, j' = 1, \cdots, L$, and

$$G_{jj'} = \begin{cases} 1 & \text{if } |j-j'| = 1 \text{ for } j = 1, \cdots, L-1 \text{ and } j' = 1, \cdots, L\,, \\ 2 & \text{if } j = L \text{ and } j' = L-1\,, \\ 0 & \text{otherwise}\,, \end{cases} \tag{A.4}$$

for $M = 2L-1$ odd, and

$$G_{jj'} = \begin{cases} 1 & \text{if } |j-j'| = 1\,, \\ 1 & \text{if } j = j' = L\,, \\ 0 & \text{otherwise}\,, \end{cases} \tag{A.5}$$

for $M = 2L$ even. Tangential LEs are obtained by replacing $\xi(t_k)$ with $\xi^{\parallel}(t_k)$ in (A.2)–(A.3).

Appendix A.1.2. Transverse Lyapunov Exponents

To compute transverse LEs, we numerically integrate the restriction of (5) to $\mathrm{Fix}(\mathbb{Z}_2)$ (given in Appendix A.1.1), together with linear equations governing the time evolution of a perturbation vector, $\xi^{\perp}(t)$, solely transverse to $\mathrm{Fix}(\mathbb{Z}_2)$. For $M = 2L-1$ odd, the transverse perturbation vector is given by

$$\begin{pmatrix} \xi_1^{\perp} \\ \xi_2^{\perp} \\ \vdots \\ \xi_{L-1}^{\perp} \end{pmatrix} = \begin{pmatrix} \xi_M - \xi_1 \\ \xi_{M-1} - \xi_2 \\ \vdots \\ \xi_{L+1} - \xi_{L-1} \end{pmatrix},$$

and $d\xi_j^{\perp}/dt$ has the same general form as (A.1), but with $j, j' = 1, \cdots, L-1$, and

$$G_{jj'} = \begin{cases} 1 & \text{if } |j-j'| = 1\,, \\ 0 & \text{otherwise}\,. \end{cases}$$

For $M = 2L$ even, the transverse perturbation vector is given by

$$\begin{pmatrix} \xi_1^{\perp} \\ \xi_2^{\perp} \\ \vdots \\ \xi_L^{\perp} \end{pmatrix} = \begin{pmatrix} \xi_M - \xi_1 \\ \xi_{M-1} - \xi_2 \\ \vdots \\ \xi_{L+1} - \xi_L \end{pmatrix},$$

and $d\xi_j^{\perp}/dt$ has the same general form as (A.1), but with $j, j' = 1, \cdots, L$, and

$$G_{jj'} = \begin{cases} 1 & \text{if } |j - j'| = 1\,, \\ -1 & \text{if } j = j' = L \\ 0 & \text{otherwise}\,. \end{cases}$$

Transverse LEs are obtained by replacing $\xi(t_k)$ with $\xi^{\perp}(t_k)$ in (A.2)–(A.3).

References

[1] M. Sargent III, M. O. Scully, W. E. Lamb Jr., Laser physics, Addison–Wesley, New York, 1974.

[2] C. O. Weiss, R. Vilaseca, Dynamics of Lasers, VCH, Weinheim, 1991.

[3] B. Krauskopf, D. Lenstra (Eds.), Fundamental issues of nonlinear laser dynamics, American Institute of Physics, 2000.

[4] H. G. Winful, L. Rahman, Phys. Rev. Lett. 65 (1990) 1575–1578.

[5] H. Adachihara, O. Hess, R. Indik, J. V. Moloney, J. Opt. Soc. Am. B 10 (1993) 496–506.

[6] R. Roy, K. S. Thornburg, Phys. Rev. Lett. 72 (1994) 2009–2012.

[7] D. Merbach, O. Hess, H. Herzel, E. Schöll, Phys. Rev. E 52 (1995) 1571–1578.

[8] S. Riyopoulos, Phys. Rev. A 66 (2002) 053820.

[9] S. Yanchuk, K. R. Schneider, L. Recke, Phys. Rev. E 69 (2004) 056221.

[10] S. Wieczorek, W. W. Chow, Opt. Commun. 246 (2005) 471–493.

[11] S. Yanchuk, A. Stefanski, T. Kapitaniak, J. Wojewoda, Phys. Rev. E 73 (2006) 016209.

[12] F. Rogister, R. Roy, Phys. Rev. Lett. 98 (2007) 104101.

[13] N. Blackbeard, H. Erzgräber, S. Wieczorek, SIAM J. Appl. Dyn. Syst. 10 (2011) 469–509.

[14] D. Botez, D. R. Scifres, Diode Laser Arrays, Cambridge University Press, 1994.

[15] M. Kanskar, F. Brunet, Phonton. Spectra http://www.photonics.com/Article.aspx?AID=39228 (2009) 496–506.

[16] T. Watanabe, M. Watanabe, Space Optical Systems and Applications (ICSOS), 2011 International Conference on (2011) 253–258.

[17] J. R. Terry, K. S. Thornburg, D. J. DeShazer, G. D. VanWiggeren, S. Zhu, P. Ashwin, R. Roy, Phys. Rev. E 59 (1999) 4036–4043.

[18] A. F. Glova, Quantum Electron. 33 (2003) 283–306.

[19] K. Otsuka, Phys. Rev. Lett. 65 (1990) 329–332.

[20] R. Li, T. Erneux, Opt. Commun. 99 (1993) 196–200.

[21] M. Silber, L. Fabiny, K. Wiesenfeld, J. Opt. Soc. Am. B 10 (1993) 1121–1129.

[22] R. Li, T. Erneux, Phys. Rev. A 49 (1994) 1301–1312.

[23] H. G. Winful, S. S. Wang, Appl. Phys. Lett. 53 (1988) 1894–1896.

[24] E. Allaria, F. T. Arecchi, A. D. Garbo, R. Meucci, Phys. Rev. Lett. 86 (2001) 791–794.

[25] R. A. Oliva, S. H. Strogatz, Int. J. Bifurcat. Chaos 11 (2001) 2359–2374.

[26] G. Kozyreff, A. G. Vladimirov, P. Mandel, Phys. Rev. E 64 (2001) 016613.

[27] F.-Y. Lin, J.-M. Liu, IEEE J. Quantum Electron. 40 (2004) 815–820.

[28] T. Heil, J. Mulet, I. Fischer, C. R. Mirasso, M. Peil, P. Colet, W. Elsässer, IEEE J. Quantum Electron. 38 (2002) 1162–1170.

[29] A. Argyris, D. Syvridis, L. Larger, V. Annovazzi-Lodi, P. Colet, I. Fischer, J. Garcia-Ojalvo, C. R. Mirasso, L. Pesquera, K. A. Shore, Nature 438 (2005) 343–346.

[30] A. Uchida, K. Amano, M. Inoue, K. Hirano, S. Naito, H. Someya, I. Oowada, T. Kurashige, M. Shiki, S. Yoshimori, K. Yoshimura, P. Davis, Nat. Photon 2 (2008) 728–732.

[31] F. T. Arecchi, G. L. Lippi, G. P. Puccioni, J. R. Tredicce, Opt. Commun. 51 (1984) 308–314.

[32] S. Wieczorek, B. Krauskopf, T. B. Simpson, D. Lenstra, Phys. Rep. 416 (2005) 1–128.

[33] A. Pikovsky, M. Rosenblum, J. Kurths, Synchronisation: a universal concept in nonlinear sciences, Cambridge University Press, 2003.

[34] P. Ru, P. K. Jakobsen, J. V. Moloney, R. A. Indik, J. Opt. Soc. Am. B 10 (1993) 507–515.

[35] H. Erzgräber, S. Wieczorek, B. Krauskopf, Phys. Rev. E 78 (2008) 066201.

[36] R. Brown, L. Kocarev, Chaos 10 (2000).

[37] M. Golubitsky, I. Stewart, The symmetry perspective—from equilibrium to chaos in phase space and physical space, Birkhäuser Verlag, 2002.

[38] I. R. Epstein, M. Golubitsky, Chaos 3 (1993).

[39] K. Josić, Phys. Rev. Lett. 80 (1998) 3053–3056.

[40] M. Golubitsky, I. Stewart, D. G. Schaeffer, Singularities and groups in bifurcation theory - volume II, Springer-Verlag, New York, 1985.

[41] L. M. Pecora, T. L. Carroll, Phys. Rev. Lett. 80 (1998) 2109–2112.

[42] J. F. Elliott, The characteristic roots of certain real symmetric matrices, Master's thesis, Univ. of Tennessee, 1953.

[43] W.-C. Yueh, Applied Mathematics E-Notes 5 (2005) 66–74.

[44] S. Wiggins, Introduction to applied nonlinear dynamical systems and chaos, Springer, New York, second edition, 2003.

[45] Y. A. Kuznetsov, Elements of applied bifurcation theory, Springer-Verlag, New York, 2004.

[46] P. Hirschberg, E. Knobloch, Physica D 62 (1993) 202–216.

[47] E. Ott, Chaos in dynamical systems, Cambridge University Press, Cambridge, 2002.

[48] E. J. Doedel, A. R. Champneys, T. F. Fairgieve, Y. A. Kuznetsov, B. Oldeman, R. Paffenroth, B. Sandstede, X. Wang, C. Zhang, AUTO-07P: Continuation and bifurcation software for ordinary differential equations, Technical Report, Concordia University, Montreal, Canada, 2007.

[49] P. Ashwin, J. Buescu, I. Stewart, Phys. Lett. A 193 (1994) 126–139.

[50] S. C. Venkataramani, B. R. Hunt, E. Ott, Phys. Rev. Lett. 77 (1996).

[51] J. Milnor, Commun. Math. Phys. 99 (1985) 177–195.

[52] J. Milnor, Commun. Math. Phys. 102 (1985) 517–519.

[53] P. Ashwin, J. Buescu, I. Stewart, Nonlinearity 9 (1996) 703–737.

[54] B. R. Hunt, E. Ott, Phys. Rev. E 54 (1996) 328–337.

[55] J. C. Sommerer, E. Ott, Nature 365 (1993) 138–140.

[56] P. Ashwin, E. Covas, R. Tavakol, Nonlinearity 12 (1999) 563–577.

[57] R. Sturman, P. Ashwin, in: G. Dangelmayr, I. Oprea (Eds.), Dynamics and bifurcation of patterns in dissipative systems, volume 12 of *B*, World Scientific, 2004, pp. 357–372.

[58] O. V. Popovych, Y. L. Maistrenko, P. A. Tass, Phys. Rev. E 71 (2005) 065201.

[59] J. D. Farmer, E. Ott, J. A. Yorke, Physica D 7 (1983) 153–180.

[60] S. Wieczorek, Phys. Rev. E 79 (2009) 036209.

[61] N. Blackbeard, H. Erzgräber, S. Wieczorek, Shear-induced chaos in lasers (SIADS multimedia), http://www.dynamicalsystems.org/pi/fr/detail?item=118, 2011.

[62] D. J. Albers, J. C. Sprott, J. P. Crutchfield, Phys. Rev. E 74 (2006) 057201.

[63] D. J. Albers, J. C. Sprott, Nonlinearity 19 (2006) 1801–1847.

[64] I. Shimada, T. Nagashima, Prog. Theor. Phys. 61 (1978) 1605–1616.

[65] G. Benettin, L. Galgani, A. Giorgilli, J.-M. Strelcyn, Meccanica 15 (1980) 9–20.

[66] G. Benettin, L. Galgani, A. Giorgilli, J.-M. Strelcyn, Meccanica 15 (1980) 21–30.